Ocean Engineering 324 (2025) 120731

Contents lists available at ScienceDirect

Ocean Engineering

journal homepage: www.elsevier.com/locate/oceaneng

Research paper

Investigation of the effect of blade angle of Archimedes spiral hydrokinetic turbine based on hydrodynamic performance and entropy production theory

Ke Song [a], Hui-Ting Huan [b], Liu-Chuang Wei [a], Chun-Xia Liu [c,*]

[a] School of Mechanical and Electrical Engineering, Kunming University, Kunming, 650214, China
[b] School of Mechano-Electronic Engineering, Xidian University, Xi'an, 710071, China
[c] School of Statistic and Mathematics, Yunnan University of Finance and Economics, Kunming, 650221, China

ARTICLE INFO

Keywords:
Archimedes spiral hydrokinetic turbine
Hydrodynamic performance
Entropy production
Blade angle

ABSTRACT

The Archimedes Spiral Hydrokinetic Turbine (ASHT) represents a novel design specifically engineered to operate in low-speed ocean currents. However, the characteristics of energy losses associated with these turbines have not yet been fully understood. This paper examines nine ASHTs with varying blade angle configurations. The analysis of the hydrodynamic performance and energy loss characteristics of these turbines, under both axial and yawed flow conditions, is conducted using computational fluid dynamics in conjunction with entropy production theory. The results indicate that ASHTs with larger blade angles can operate across a broader range of tip speed ratios, achieving optimal power performance at higher tip speed ratios and generating greater thrust. In contrast, variable blade angle configurations demonstrate higher peak power but exhibit lower thrust and a narrower operating range of yaw angles compared to their fixed blade angle counterparts. The wake region behind the ASHT with a larger blade angle is characterized by a more extensive low-velocity area and a prominent hub recirculation zone. The energy loss occurring in the wake region is primarily attributed to the vortices generated at the tip and hub, with hub vortices being the main contributors to increased entropy production rates for configurations with larger blade angles. Under yawed flow conditions, an increase in yaw angle results in significant reductions in power and thrust, altered wake structures, and an increase in total entropy production. These findings provide crucial insights for the design and optimization of ASHTs, ultimately contributing to the development of more efficient and cost-effective ocean current power generation systems.

1. Introduction

In the contemporary context of the global energy transition, the pursuit of sustainable and clean energy sources is crucial for the long-term development of the industrial sector. Among renewable energy resources, ocean current energy has emerged as a promising alternative to fossil fuels. Its remarkable advantages—abundance, cost-effectiveness, renewability, and environmental friendliness (Olabi and Abdelkareem, 2022; Li et al., 2022)—not only provide a new direction for energy diversification but also expand the operational scope of various offshore platforms. The utilization of ocean current energy has effectively extended the deployment of these platforms from coastal shallows to deeper waters (Laws and Epps, 2016), facilitating more comprehensive ocean exploration and resource exploitation. Simultaneously, in the field of ocean observation, there is an urgent need to reduce costs and enhance the efficiency of sensor deployment. Harnessing local ocean current energy for different platforms has thus become a research hotspot. Hydrokinetic turbines play a crucial role in this process, as they are well-equipped to supply power to multifunctional platforms involved in offshore drilling, oil extraction, monitoring, navigation, and construction. However, the vast expanse of the ocean presents a challenge: high-speed current areas are limited, and extracting local ocean current energy, especially in low-flow-speed regions, remains a formidable task.

For the development of a power generation system for offshore platforms, the turbine's ability to self-start in low-ocean-current conditions is a critical factor. Lift-type hydrokinetic turbines, which include horizontal axis hydrodynamic turbines (HAHTs) and some vertical axis

* Corresponding author.
E-mail address: lcx13099971218@163.com (C.-X. Liu).

https://doi.org/10.1016/j.oceaneng.2025.120731
Received 20 October 2024; Received in revised form 16 February 2025; Accepted 17 February 2025
Available online 22 February 2025

hydrodynamic turbines (VAHTs), have reached the commercialization stage (Allmark et al., 2020; Nunes et al., 2020). Nevertheless, these turbines are optimized for shallow, high-current-speed areas and face significant difficulties in self-starting under low-current conditions (Satrio and Utama, 2021). As a result, they are not suitable for power generation in many offshore regions. Therefore, the development and application of hydrokinetic turbines that can self-start and operate efficiently at low speeds are essential for ensuring a stable power supply to offshore platforms (Gao et al., 2020). The Archimedes spiral hydrodynamic turbine (ASHT) represents a significant advancement in this field. Initially designed for low-head hydropower stations, its application has now been extended to free-flowing water environments. The ASHT is distinct from traditional HAHTs in its design principles. While traditional HAHTs often rely on the Blade Element Momentum (BEM) theory, the ASHT is based on the principles of the Archimedes spiral design. Its unique configuration of multiple interlocking screw blades is a key feature. The number of blades is crucial: too few blades would reduce the force-transformation area, leading to lower torque; conversely, an excessive number of blades would create a solid obstruction, increasing mass and inertia, thus decreasing torque output (Bakırcı and Yılmaz, 2018). Research by Suntivarakorn et al. (2016) has shown that an ASHT with three blades can optimize torque and overall performance.

Importantly, the ASHT is recognized for its ability to utilize drag force for energy production, classifying it as a drag-type hydrokinetic turbine. This inherent characteristic enables it to operate effectively in low-ocean-current conditions. In deep-sea environments, where the average current speed is generally low, traditional lift-type turbines struggle to start and generate power. In contrast, the ASHT can start smoothly and maintain a relatively high power coefficient. Moreover, the blades of the ASHT possess additional advantages. They are relatively easy to construct from sheet metal, simplifying the manufacturing process and potentially reducing production costs. This contrasts with the more complex hydrofoil-shaped blades of a conventional HAHT, which often require intricate manufacturing techniques. Additionally, the helical blade design of the ASHT exhibits fish-friendly characteristics, making it less likely to harm marine life. This makes the ASHT an even more ideal candidate for power generation in offshore platforms across different ocean regions, especially in deep-sea areas with low-speed currents. It has the potential to significantly improve the power supply situation of deep-sea observation equipment, reducing reliance on traditional power-supply methods such as research vessels and cable nodes, which are costly and environmentally impactful. Fig. 1 shows a schematic of the ASHT deep-sea power generation system. By providing a stable power source, the ASHT can support the long-term operation of offshore platforms, facilitating more in-depth ocean research and resource exploration.

Fig. 1. Schematic of ASHT deep sea power generation system.

From another perspective, understanding energy loss is crucial for optimizing turbine performance. Traditional hydrodynamics suggests that energy loss is closely associated with unstable flow. However, accurately quantifying the magnitude and distribution of this energy loss remains a significant challenge. This uncertainty has driven researchers to explore more advanced methods to gain a deeper insight into the mechanisms of energy dissipation in turbines. In recent years, entropy production theory, grounded in the principles of the second law of thermodynamics, has emerged as a powerful tool in the turbine industry. This theory has garnered considerable attention in various studies aimed at examining energy loss from a thermodynamic perspective. Unlike conventional methods, which often provide only a macroscopic view of energy loss, the entropy production method offers a more comprehensive and detailed approach. It serves as an effective instrument for assessing irreversible losses, allowing researchers to investigate the root causes of inefficiencies within turbine systems.

One of the primary advantages of entropy production theory is its capacity to analyze energy loss at the level of individual components under specific operating conditions. This component-specific analysis is essential for identifying areas of high energy dissipation within complex turbine systems. By pinpointing these areas, engineers and researchers can develop targeted strategies to enhance turbine design and operation, ultimately improving overall performance. Moreover, the entropy production method can reveal the locations and spatial patterns of energy losses. This spatial information is invaluable for understanding how energy is dissipated throughout the turbine, which can aid in optimizing the turbine's geometry and flow path. For instance, Nazeryan and Lakzian (2018) conducted a comparative analysis of Wells turbines with blades of uniform thickness versus those with variable thickness, focusing on entropy generation. Ghisu et al. (2018) revisited the principles governing entropy generation in fluid flows, providing insights into isolated airfoils and Wells turbines. Guo and Wang (2023) applied entropy production theory to assess energy losses in hydrokinetic turbine hydrofoils, particularly under dynamic stall conditions. Yu et al. (2021) investigated a Francis turbine operating under various conditions, using the entropy production method to illustrate the distribution of the local entropy production rate within the draft tube. Yang et al. (2022) explored energy loss in axial-flow pump systems through entropy production theory. Wang et al. (2023a,b) utilized numerical simulations to analyze energy loss characteristics in a ducted hydrokinetic turbine.

Currently, the ASHT has garnered increasing attention in recent years due to its potential for harnessing hydrokinetic energy, particularly in low-speed flow environments. Previous research on ASHTs has made significant contributions, yet it also has its limitations. Suntivarakorn et al. (2016) enhanced the efficiency of an ASHT, demonstrating its superiority in electricity generation from low-current conditions compared to a HAHT. This work was pivotal as it showcased the potential of ASHTs in low-current environments, which are prevalent in many natural water bodies. However, it may not have thoroughly examined the long-term stability and reliability of the enhanced efficiency under the complex conditions encountered in real-world scenarios. Monatrakul and Suntivarakorn (2017) employed modeling and Computational Fluid Dynamics (CFD) analysis to investigate the impact of blade angle on ASHT efficiency, discovering that a collection chamber could enhance performance. The significance of this study lies in its provision of a practical method for improving turbine efficiency. Nevertheless, the research may have been confined to a specific range of blade angles and flow conditions, lacking a more comprehensive exploration of the intricate interactions between blade angles, collection chambers, and various flow scenarios. Song and Kang (2022a,b) explored the fluid-structure coupling performance of an ASHT through simulations, identifying the blade root region as the area of highest stress concentration. This finding is crucial for understanding the structural integrity and potential failure points of ASHTs. However, the simulation-based approach may not fully account for all real-world factors that could influence fluid-structure interactions, such as material fatigue under long-term cyclic loading. Monatrakul et al. (2023) compared the power performance of an ASHT with a HAHT, revealing that the ASHT maintained efficiency at water speeds between 1 and 2 m/s, while the three-blade HAHT required higher speeds. This comparison is valuable for selecting the appropriate turbine type for varying flow conditions. However, the study may not have considered the influence of other environmental factors on the performance differences observed. Zhang et al. (2023) analyzed the blockage effects on ASHTs in comparison with two other hydrokinetic turbines and evaluated various blockage correction techniques. Their work is significant for enhancing the accuracy of experimental studies on ASHTs. However, the proposed correction techniques may require further validation through large-scale field experiments across different types of water channels and flow conditions. Badawy et al. (2023) examined the impact of blade hydrofoil design on ASHT efficiency. This research is important for optimizing blade design to enhance overall turbine performance. However, it may have focused on a limited number of hydrofoil designs, and the results might not be universally applicable to all ASHT models. Song et al. (2024) compared the ASHT with its ducted configuration (DASHT) and found that the DASHT exhibited a significant performance advantage, with a 122% increase in power coefficient. This study provided new insights into the potential of ducted ASHTs. However, it may not have addressed the economic feasibility and practical challenges associated with implementing DASHT in large-scale applications. Zhang et al. (2024) experimentally tested ASHT performance under yawed conditions and proposed optimization strategies. This research is valuable for enhancing ASHT efficiency in real-world flow situations where yawed flow is common. However, the experimental conditions may not fully represent the extreme and complex yawed flow conditions found in actual ocean environments. Furthermore, while previous studies have explored various aspects of ASHTs, most research has concentrated on individual factors such as efficiency, power performance, or blockage effects. The specific mechanisms by which blade angle influences ASHT performance, particularly the underlying hydrodynamic and energy-loss mechanisms, remain unclear. There is a notable lack of in-depth understanding regarding the complex flow phenomena associated with changes in blade angle.

In light of the aforementioned points, this paper aims to provide a comprehensive description of the effect of blade angle on ASHT performance. It also seeks to elucidate the underlying reasons for variations in hydrodynamic characteristics, with a particular emphasis on entropy production in ASHTs under both axial and yawed flow conditions. The novelty of this study lies in its focus on entropy production analysis in ASHTs across different flow conditions. By considering entropy production, this paper aims to offer a more profound understanding of the energy-loss mechanisms related to blade angle, providing a fresh perspective on the performance evaluation of ASHTs. The findings of this paper can contribute to engineering practice in several ways. Firstly, understanding the effect of blade angle on performance and entropy production can assist designers in optimizing ASHT. For instance, it can guide the selection of the most suitable blade angle for various flow conditions to minimize energy losses and maximize power generation. Secondly, insights into hydrodynamic characteristics can aid in the development of more efficient and reliable ASHT-based power generation systems, applicable in diverse hydrokinetic energy-harvesting scenarios, such as ocean currents and rivers. This research addresses the gap in understanding the complex relationship between blade angle, hydrodynamics, and energy loss in ASHTs, providing a more robust theoretical foundation for the practical application of ASHTs. The structure of this paper is organized as follows: Section 2 introduces the governing equation and the method for calculating entropy production. Following this, Section 3 provides a detailed description of the simulation model which includes the hydrodynamic coefficients, the computational domain and mesh, the numerical methods utilized, and the validation process. Sections 4 and 5 examine the performance of the ASHT analysis under both axial flow and yawed flow conditions, including assessments of hydrodynamics, entropy production, and the flow field. Section 6 presents the discusses. Finally, Section 7 presents the concluding remarks.

2. Governing equations and entropy production theory

The Reynolds Averaging Navier-Stokes (RANS) method was adopted in this simulation, and the governing equations are shown as follows:

$$\frac{\partial \overline{u}_i}{\partial x_i}=0 \tag{1}$$

$$\rho\left(\frac{\partial \overline{u}_i}{\partial t}+u_j\frac{\partial \overline{u}_i}{\partial x_j}\right)=-\frac{\partial \overline{p}}{\partial x_i}+\mu\frac{\partial}{\partial x_j}\left(\frac{\partial \overline{u}_i}{\partial x_j}+\frac{\partial \overline{u}_j}{\partial x_i}\right)+\frac{\partial \tau_{ij}}{\partial x_j} \tag{2}$$

$$\tau_{ij}=-\rho\overline{u_i'u_j'} \tag{3}$$

$$-\rho\overline{u_i'u_j'}=\mu_t\left(\frac{\partial \overline{u}_i}{\partial x_j}+\frac{\partial \overline{u}_j}{\partial x_i}\right)-\frac{2}{3}\mu_t\frac{\partial \overline{u}_k}{\partial x_k}\delta_{ij}-\frac{2}{3}\rho k\delta_{ij} \tag{4}$$

here, $\overline{u}$ represents time-averaged velocity (m/s), t is time (s), ρ is fluid density (kg/m^3), $\overline{p}$ is average pressure (Pa), μ denotes molecular dynamic viscosity (N·s/m^2) and μ_t denotes the eddy viscosity (N·s/m^2), τ_{ij} denotes Reynolds stress tensor (Pa), δ_{ij} denotes the Kronecker delta operator. The subscripts (i, j, k) represent three directions in Cartesian coordinates.

From a thermodynamic standpoint, the incoming water interacts with an ASHT, transforming a portion of its kinetic energy into mechanical energy. This transformation is inherently irreversible, resulting in the production of entropy, as dictated by the second law of thermodynamics. The entropy production is directly linked to the loss of energy, which provides a quantitative measure of energy dissipation within an ASHT system. The equation governing entropy transport in incompressible fluid flows is presented below (Herwig and Kock, 2007):

$$\rho\left(\frac{\partial s}{\partial t}+u\frac{\partial s}{\partial x}+v\frac{\partial s}{\partial y}+w\frac{\partial s}{\partial z}\right)=-div\left(\frac{\vec{q}}{T}\right)+\frac{\Phi}{T}+\frac{\Phi_\Theta}{T^2} \tag{5}$$

here, u, v and w are instantaneous velocity, s represents specific entropy per unit mass [J/(kg·K)], q is heat flux (W/m^2), T represents local temperature (K), Φ and Φ_Θ denotes dissipation function.

Using the Reynolds time-averaging approach, instantaneous variables can be decomposed into two distinct components: a time-averaged portion and a fluctuating portion:

$$s=\overline{s}+s' \tag{6}$$

$$u=\overline{u}+u' \tag{7}$$

here, $\overline{s}$ is time-average specific entropy, s' is fluctuating specific entropy, u' is fluctuating velocity.

Employ Reynolds time-average method, Eq. (5) can be transformed into follows:

$$\rho\left[\left(\frac{\partial\overline{s}}{\partial t}+\overline{u}\frac{\partial\overline{s}}{\partial x}+\overline{v}\frac{\partial\overline{s}}{\partial y}+\overline{w}\frac{\partial\overline{s}}{\partial z}\right)+\left(\frac{\partial\overline{u's'}}{\partial x}+\frac{\partial\overline{v's'}}{\partial y}+\frac{\partial\overline{w's'}}{\partial z}\right)\right]=-div\overline{\left(\frac{\vec{q}}{T}\right)}+\underbrace{\frac{\overline{\Phi}}{T}}_{\mathrm{I}}+\underbrace{\frac{\Phi_\Theta}{T^2}}_{\mathrm{II}} \tag{8}$$

On the right-hand side of Eq. (8), the first dissipation term (I) corresponds to the entropy production rate (EPR) caused by viscous effects within the fluid, while the second dissipation term (II) accounts for the EPR resulting from irreversible heat transfer processes. In the context of ASHT flows, temperature fluctuations are minimal, allowing the thermodynamic system to be approximated as one operating under constant temperature conditions (Wang et al., 2023a,b).

The dissipation function term I can be written as follows:

$$\frac{\Phi}{T}=\frac{\mu}{T}\left[2\left\{\left(\frac{\partial u}{\partial x}\right)^2+\left(\frac{\partial v}{\partial y}\right)^2+\left(\frac{\partial w}{\partial z}\right)^2\right\}+\left(\frac{\partial u}{\partial y}+\frac{\partial v}{\partial x}\right)^2+\left(\frac{\partial u}{\partial z}+\frac{\partial w}{\partial x}\right)^2+\left(\frac{\partial v}{\partial z}+\frac{\partial w}{\partial y}\right)^2\right] \tag{9}$$

By applying the Reynolds time-averaging method, Eq. (9) can be reformulated as Eq. (10). This equation can then be separated into two distinct components: a time-averaged section (Eq. (11)) and a fluctuating section (Eq. (12)):

$$\frac{\overline{\Phi}}{T}=\frac{\mu}{T}\left[\begin{array}{l}2\left\{\left(\frac{\partial\overline{u}}{\partial x}\right)^2+\left(\frac{\partial\overline{v}}{\partial y}\right)^2+\left(\frac{\partial\overline{w}}{\partial z}\right)^2\right\}+\left(\frac{\partial\overline{u}}{\partial y}+\frac{\partial\overline{v}}{\partial x}\right)^2+\left(\frac{\partial\overline{u}}{\partial z}+\frac{\partial\overline{w}}{\partial x}\right)^2+\left(\frac{\partial\overline{v}}{\partial z}+\frac{\partial\overline{w}}{\partial y}\right)^2+\\ 2\left\{\left(\frac{\partial u'}{\partial x}\right)^2+\left(\frac{\partial v'}{\partial y}\right)^2+\left(\frac{\partial w'}{\partial z}\right)^2\right\}+\left(\frac{\partial u'}{\partial y}+\frac{\partial v'}{\partial x}\right)^2+\left(\frac{\partial u'}{\partial z}+\frac{\partial w'}{\partial x}\right)^2+\left(\frac{\partial v'}{\partial z}+\frac{\partial w'}{\partial y}\right)^2\end{array}\right] \tag{10}$$

$$S_{pro\,VD}=\frac{\mu_{eff}}{T}\left[\left(\frac{\partial\overline{u}}{\partial y}+\frac{\partial\overline{v}}{\partial x}\right)^2+\left(\frac{\partial\overline{u}}{\partial z}+\frac{\partial\overline{w}}{\partial x}\right)^2+\left(\frac{\partial\overline{v}}{\partial z}+\frac{\partial\overline{w}}{\partial y}\right)^2\right]+\frac{2\mu_{eff}}{T}\left[\left(\frac{\partial\overline{u}}{\partial x}\right)^2+\left(\frac{\partial\overline{v}}{\partial y}\right)^2+\left(\frac{\partial\overline{w}}{\partial z}\right)^2\right] \tag{11}$$

$$S_{proTD}=\frac{\mu_{eff}}{T}\left[\left(\frac{\partial u'}{\partial y}+\frac{\partial v'}{\partial x}\right)^2+\left(\frac{\partial u'}{\partial z}+\frac{\partial w'}{\partial x}\right)^2+\left(\frac{\partial v'}{\partial z}+\frac{\partial w'}{\partial y}\right)^2\right]+\frac{2\mu_{eff}}{T}\left[\left(\frac{\partial u'}{\partial x}\right)^2+\left(\frac{\partial v'}{\partial y}\right)^2+\left(\frac{\partial w'}{\partial z}\right)^2\right] \tag{12}$$

$$\mu_{eff}=\mu+\mu_t \tag{13}$$

here, S_{proVD} represents the entropy production rate by direct dissipation (EPDD) [W/(m3·K)], which is induced by time-averaged velocity, S_{proTD} represents the entropy production rate by turbulent dissipation (EPTD) [W/(m3·K)], which is induced by fluctuating velocity.

In the Reynolds time-averaging approach, the fluctuating velocity component is not directly computed. Instead, the entropy production due to turbulence dissipation is estimated using an approximation function integrated with a turbulence model. For instance, in the case of the k-ω turbulence model, the entropy production due to dissipation can be determined through the following function (Kock and Herwig, 2004):

$$S_{pro\,TD}=\delta\frac{\rho\omega k}{T} \tag{14}$$

here, δ denotes the experimental constant of the SST k-ω turbulent model, valued at 0.09 (Li et al., 2017); ω indicates the specific dissipation rate; and k represents turbulence kinetic energy.

The entropy production due to turbulence dissipation and due to dissipation can be obtained by EPR integrating with the computational domain:

$$S_{VD}=\int_V S_{proVD}dV \tag{15}$$

$$S_{TD}=\int_V S_{proTD}dV \tag{16}$$

Therefore, the total entropy production can be written as follows:

$$S_{TEP}=S_{VD}+S_{VD} \tag{17}$$

here, S_{VD} refers to the entropy production resulting from direct dissipation (W/m^3); S_{TD} indicates the entropy production caused by turbulent dissipation (W/m^3); and S_{TEP} represents the total entropy

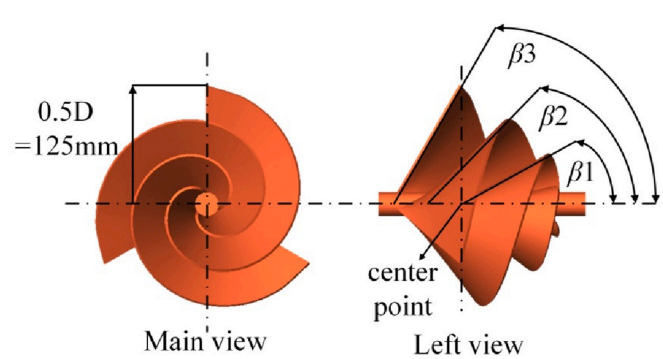

Fig. 2. Schematic view of an ASHT.

production (W/m^3).

Based on the previously discussed theoretical framework, the energy loss within a system can be quantitatively determined through integration. Additionally, the spatial distribution of this energy loss can be effectively visualized using the entropy production method.

3. Numerical computational model

3.1. CFD modeling

This research utilizes the steady incompressible Reynolds-Averaged Navier-Stokes (RANS) equations in conjunction with the Shear Stress Transport *k*-*ω* (SST *k*-*ω*) turbulence model (Menter, 1994) to perform in-depth and effective simulations of flow dynamics. The SST *k*-*ω* model has proven to be superior in calculating complex flows (Tampier et al., 2017; Yang et al., 2021; Song and Yang, 2021; Song and Kang, 2022a,b). Its capability to accurately capture the behavior of turbulent flows, particularly in scenarios involving flow separation and strong pressure gradients, makes it especially suitable for hydrodynamic simulations of turbines. In the context of turbine flow simulations, the SST *k*-*ω* model effectively describes flow characteristics near the turbine blades, including the formation and development of boundary layers and wake regions, which are crucial for accurately predicting turbine performance. For pressure-velocity coupling, the COUPLED scheme is employed. This scheme effectively manages the interaction between pressure and velocity fields, ensuring the accuracy and consistency of simulation results. To maintain high computational precision, a second-order upwind discretization method was employed for calculating the convective flux across all cell surfaces. The computational fluid dynamics (CFD) simulations were halted under two conditions: either when the residuals of all governing equations dropped to 10^{-5}, or when the simulation completed 1000 iterations. Preliminary evaluations confirmed that these stopping criteria were adequate to guarantee convergence. Additionally, all simulations were conducted using double-precision arithmetic to minimize rounding errors during the iterative computations.

3.2. Geometry

In this paper, a total of nine ASHTs with different blade angles have been designed and created using SolidWorks software. Each ASHT features three blades with a diameter of 250 mm. The shaft has a diameter of 25 mm, while the thickness of the blades is 3 mm. Additionally, each ASHT features three unique blade angles ($\beta 1$, $\beta 2$, and $\beta 3$). The selected angles of 15°, 30°, 45°, 60°, 75°, and 90° were used to create nine different ASHT configurations, as illustrated in Fig. 2. To distinguish between the various ASHT cases based on blade angles, a notation system "x-x-x" is utilized (for instance, "60-75-90" indicates an ASHT where $\beta 1 = 60°$, $\beta 2 = 75°$, and $\beta 3 = 90°$). Furthermore, ASHTs can also be classified into two categories depending on how the blade angles are distributed: (fixed-angle and variable-angle configuration). In a fixed-angle setup, all three blade angles are identical, while in a variable-angle setup, the angles gradually rise from $\beta 1$ to $\beta 3$. Among the nine configurations, the following have fixed blade angles: 30-30-30, 45-45-45, 60-60-60, 75-75-75, and 90-90-90. In contrast, the configurations 15-30-45, 30-45-60, 45-60-75, and 60-75-90 exhibit variable blade angles.

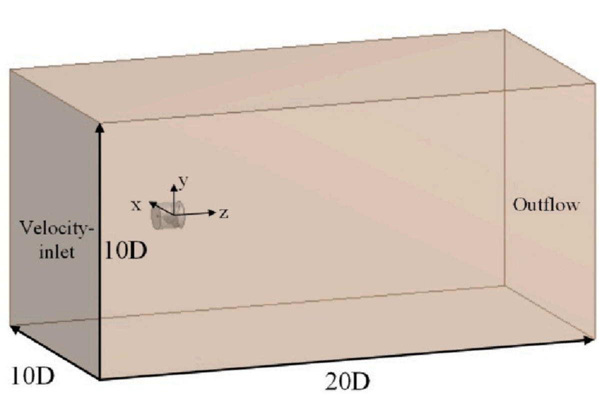

Fig. 3. Computational domain of an AHST.

The performance of an ASHT was defined by power coefficient (C_P), thrust coefficient (C_T) and torque coefficient (C_M) whose expression is shown as follows:

$$C_P = \frac{P}{0.5\rho A V_0^3} \tag{18}$$

$$C_T = \frac{T}{0.5\rho A V_0^2} \tag{19}$$

$$C_M = \frac{M}{0.5\rho A V_0^2 R} \tag{20}$$

The tip speed ratio (*TSR*) illustrates the connection between the velocity of the flow and the rotational speed of the turbine. This relationship can be expressed as follows:

$$TSR = \frac{\pi n R}{30 V_0} \tag{21}$$

here, T is the axis thrust (N) of turbine, P represents the power output (W) of turbine, M represents the torque (N·m) of turbine, V_0 is the water speed (m/s), A is the sweep area of turbine (m^2), n is the rotational speed of turbine (rpm), and R is the radius of turbine.

3.3. Computational domain

Fig. 3 illustrates the computational domain, which features a well-defined coordinate system comprising both a stationary domain and a rotating domain. To simulate the turbine's rotation relative to the stationary domain, the Moving Reference Frame (MRF) model is employed. The rotating domain is designed in a cylindrical shape, allowing for relative slip at the interfaces between the rotating and stationary domains. This relative slip is essential for ensuring the efficient transfer of flow field information, which is necessary for accurately simulating the interaction between the rotating turbine and the stationary fluid within the domain. The size of the rotating domain is intentionally set to be slightly larger than the length of the shaft and the diameter of the turbine. This sizing strategy minimizes the influence of boundary effects on the turbine flow field, thereby providing a more realistic simulation environment.

A uniform water velocity (V_0) of 0.5 m/s is specified at the inlet of the computational domain. Establishing a consistent inlet velocity is a common practice in fluid dynamics simulations, as it simplifies the analysis and allows for a focused examination of flow behavior within the domain. The outlet is defined as an outflow boundary condition, enabling the fluid to exit the domain smoothly without introducing additional artificial effects. The center of the turbine is positioned at a distance of 5D from the inlet and 15D from the outlet. This positioning is informed by previous research and empirical knowledge, ensuring that the turbine is located in a region where the flow is fully developed, thus minimizing the influence of the inlet and outlet boundaries on the turbine flow field. A no-slip condition is applied to the surface of the turbine, aligning with the physical reality that fluid adheres to solid surfaces. Conversely, the boundary surrounding the stationary domain is designated with a symmetry condition, which reduces computational complexity while maintaining the integrity of the flow field simulation.

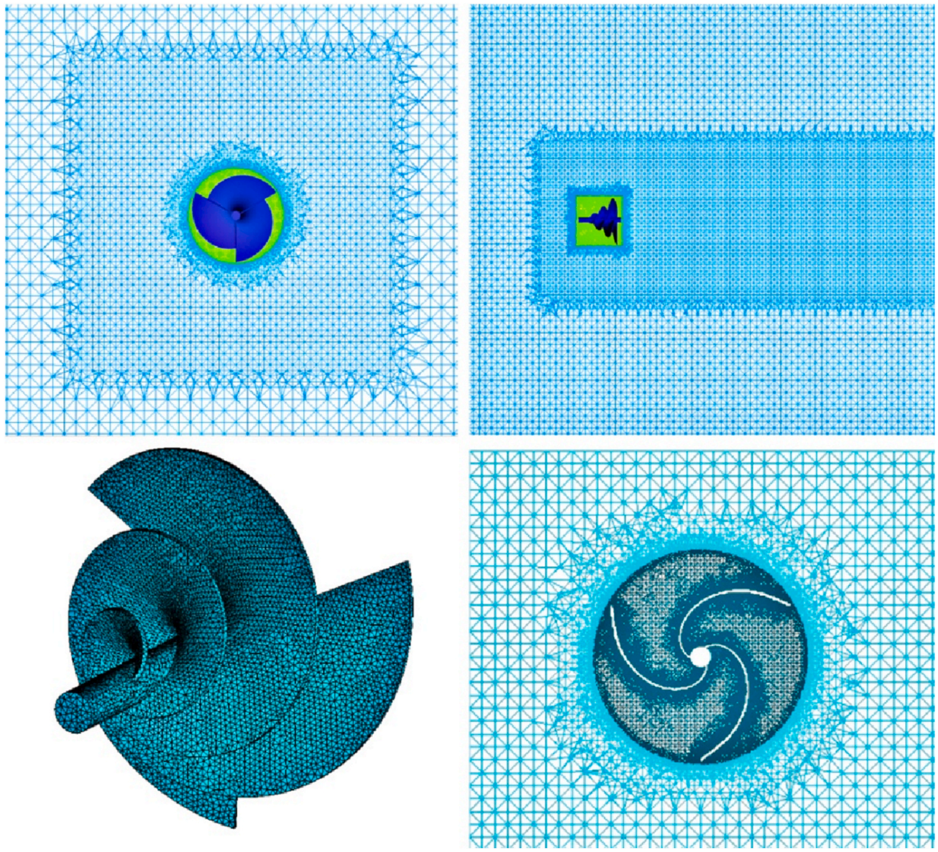

Fig. 4. Volume mesh and surface mesh around the ASHT.

Table 1
Power coefficients and relative errors for different mesh sizes.

Mesh	Total Cells	C_P	Relative error%
1	2579642	0.2298	3.12
2	3251566	0.2342	1.26
3	3819823	0.2348	1.01
4	4389145	0.2365	0.29
5	5023764	0.2372	0
6	5627891	0.2373	0.04
7	6342378	0.2372	0

3.4. Computational mesh

Unstructured meshes are utilized in this study due to their automatic generation capabilities, offering a more economical option (Lawson et al., 2011). However, it is crucial to meticulously control mesh quality factors such as orthogonality, skewness, and aspect ratio, particularly concerning mesh density. These factors significantly impact the accuracy of simulation results. For instance, high skewness values can lead to numerical errors and an inaccurate representation of the flow field. Research indicates that when using the SST *k-ω* model, it is advisable to maintain y + values at 15 or lower (Moshfeghi et al., 2012). y+ is a non-dimensional parameter representing the distance from the wall in terms of the turbulent boundary layer. Keeping a low y + value ensures that the first mesh layer resides within the viscous sublayer, which is essential for the accurate application of the SST *k-ω* model near the wall. To enhance the discretization of the boundary layer, a smooth transition algorithm is applied, utilizing ten prism layers. Fig. 4 presents the volume mesh and surface mesh details around an ASHT. Assuming an incoming velocity of 0.5 m/s and a reference length equal to the rotor diameter, the Reynolds number (*Re*) is approximately 1.2×10^5.

The height of the first layer is set at 0.045 mm (The maximum y + value is restricted to be in the range recognized for the viscous sublayer (y+ <3)), with a growth rate of 1.10. This approach improves the resolution of the boundary layer by reducing the dimensional difference between the final prism layer and the initial polyhedral element. A well-resolved boundary layer is vital for accurately capturing flow behavior near the turbine blades, including boundary layer separation and vortex formation. Moreover, accurately simulating the flow pattern necessitates careful consideration. Mesh refinement is applied near the blade to ensure simulation accuracy (Moshfeghi et al., 2017; Al-Dabbagh and Yuce, 2019). The region adjacent to the blade is critical, as it experiences

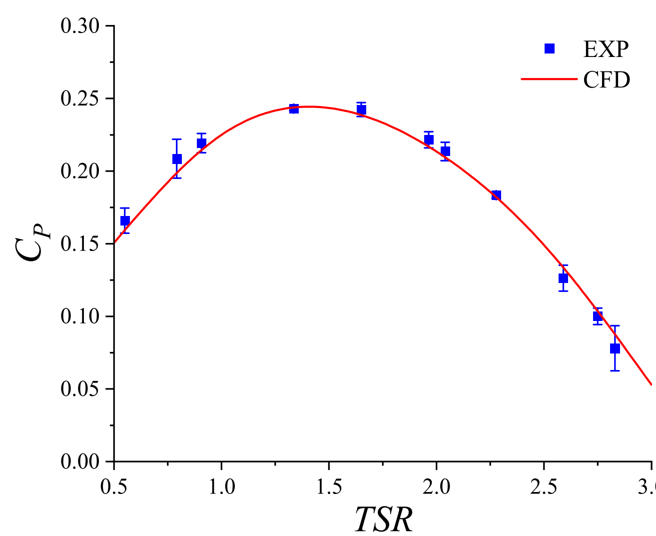

Fig. 5. Validation with experimental results.

complex flow phenomena, such as high-velocity gradients and flow separation. Refining the mesh in this area allows for better resolution of these intricate flow features, thereby enhancing simulation accuracy. Mesh refinement is particularly concentrated around the rotor and the downstream wake region to ensure precise simulations.

3.5. Numerical uncertainty

A mesh independence analysis was conducted to verify that the accuracy of the results remains unaffected by variations in element size. For this purpose, the 30-45-60 configuration (at $TSR = 1.5$) was selected as a representative case to examine the influence of mesh refinement. The mesh resolution was progressively enhanced, resulting in total element counts of 2,579,642; 3,251,566; 3,819,823; 4,389,145; 5,023,764; 5,627,891; and 6,342,378, as detailed in Table 1. Throughout these simulations, the y + value was consistently maintained y+ <3 to ensure boundary layer resolution. By comparing these results across different mesh sets, we can evaluate the impact of mesh resolution on simulation results. The findings indicate only slight variations after cell number reach 5million, suggesting that further improvements in mesh resolution would have minimal effects on the results of the CFD analysis. To enhance simulation efficiency, the 6,342,378 mesh configuration (with 2,543,901 million in the rotating domain) is selected for subsequent numerical simulations.

3.6. Validation

To validate the accuracy of the computational results, a comparative analysis was conducted between the power coefficients of the 30-45-60 rotor configuration obtained from steady-state RANS CFD simulations and the experiment reported by Kamal et al. (2022), as shown in Fig. 5. The data reveals an excellent correlation between the predictions of the current RANS-based CFD model and the previously published findings across the entire operational spectrum, with only minor variations observed. Specifically, the peak power coefficient deviation between this study and Kamal et al. (2022) was found to be within +1.37%, indicating a high degree of consistency between the two studies. These variations may arise from differences in testing equipment and environmental factors. Additionally, the exclusion of mechanical friction in the numerical simulation and potential errors in the experimental apparatus could also contribute to these discrepancies. In summary, the numerical approach employed in this study has produced results that demonstrate a satisfactory level of accuracy.

4. Results in axial flow

4.1. Power, thrust and pressure

When an ASHT undergoes rotational motion under hydrodynamic forces, a portion of the kinetic energy from the water is converted into mechanical energy, a process analogous to that observed in traditional HAHTs. The performance of ASHTs, quantified by the power coefficient (C_P) and thrust coefficient (C_T), is influenced by the tip speed ratio (*TSR*), as illustrated in Fig. 6. The trends in this figure reveal that C_P values for all ASHT configurations initially increase with *TSR* before reaching a peak and subsequently declining, a behavior consistent with conventional HAHTs. This pattern can be attributed to the balance between energy extraction efficiency and flow separation effects, which are well-documented in turbine aerodynamics. In contrast, C_T values exhibit a consistent decline with increasing *TSR* across all configurations, suggesting a reduction in hydrodynamic drag as the rotational speed increases relative to the incoming flow velocity. Among the nine ASHT designs evaluated, the 60-75-90 configuration achieves the highest peak C_P, while the 30-30-30 design records the lowest. This disparity highlights the critical role of blade angle in determining energy extraction efficiency. Specifically, ASHTs with larger blade angles operate over a broader *TSR* range and attain peak C_P at higher TSR values. For instance, the 90-90-90 configuration, which features the largest blade angle, demonstrates the widest *TSR* span and reaches its peak C_P at the highest *TSR* value. This behavior can be explained by the increased interaction time between the blades and the incoming flow, which enhances energy capture at higher rotational speeds. Conversely, configurations with smaller blade angles, such as 30-30-30, exhibit a narrower operational range and lower peak C_P, likely due to reduced flow interaction and energy extraction potential. Furthermore, ASHTs with variable blade angles (e.g., 15-30-45, 30-45-60, 45-60-75, and 60-75-90) consistently achieve higher peak C_P values compared to their fixed blade angle counterparts (e.g., 30-30-30, 45-45-45, 60-60-60, and 75-75-75). This suggests that variable blade angles optimize energy extraction by adapting to local flow conditions, thereby mitigating losses associated with fixed geometries. Additionally, a strong correlation between blade angle and C_T values is observed, with larger blade angles generally yielding higher thrust coefficients. The 90-90-90 configuration, for example, exhibits the highest C_T among all designs, reflecting the increased hydrodynamic forces acting on the blades. This trend aligns with that larger blade angles result in greater flow obstruction and higher drag forces. The observed performance variations can be attributed to differences in flow dynamics around the ASHT blades, which are directly influenced by blade angle. Smaller blade angles allow for less

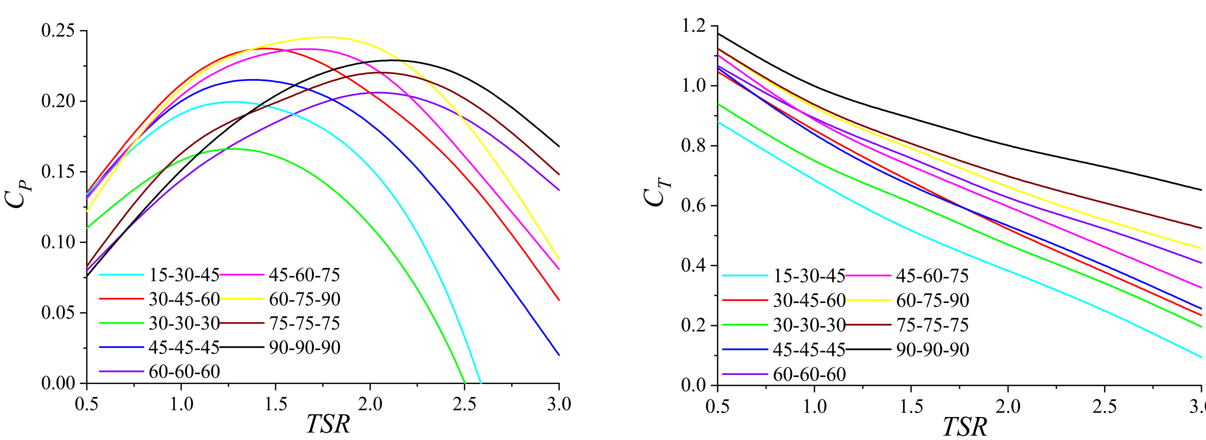

(a) C_P **(b)** C_T

Fig. 6. C_P and C_T versus *TSR* curves for the ASHTs in axial flow.

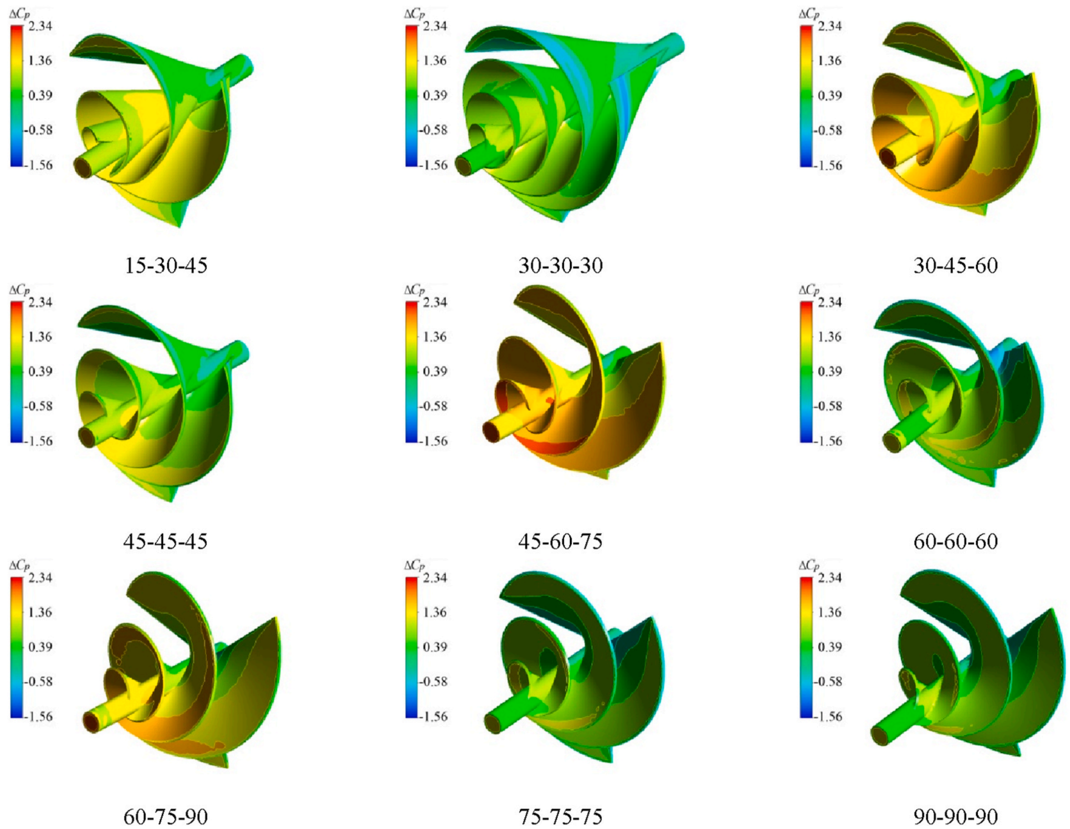

Fig. 7. Pressure coefficient ($\Delta C_p = \frac{p}{0.5\rho V_0^2}$) distribution on the ASHTs in axial flow.

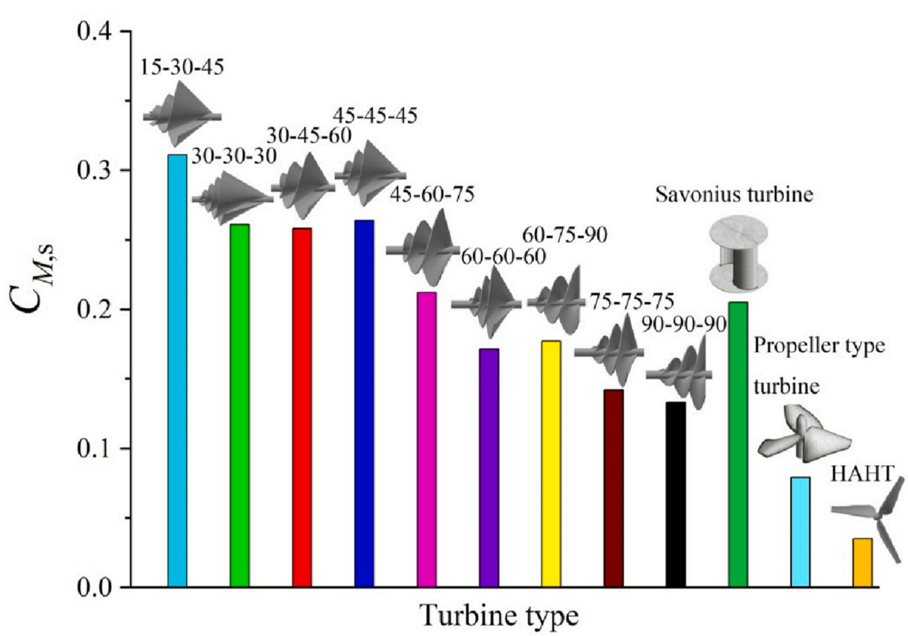

Fig. 8. Comparison of starting torque between nine ASHTs and other hydrokinetic turbines.

obstructed flow through the turbine, reducing drag but also limiting energy extraction. In contrast, larger blade angles enhance energy capture by increasing flow interaction but at the cost of higher thrust and drag. These findings underscore the importance of blade angle optimization in ASHT design, as it directly impacts both energy extraction efficiency and structural loading.

The pressure coefficient (ΔC_p) for nine ASHTs at a *TSR* of 1.5 is depicted in Fig. 7. The dynamics of ASHTs are significantly influenced by the pressure differentials generated across the blades, which are essential for the generation of torque and thrust. Specifically, the pressure side of the blade experiences higher pressure, while the suction side is characterized by lower pressure. This pressure difference results in an axial drag force on the rotor, facilitating the conversion of hydrodynamic energy into mechanical energy. This mechanism aligns with the principles observed in traditional hydrokinetic turbines, where pressure differentials serve as a primary driver of rotor motion. A notable aspect of the pressure distribution is the gradual movement of high- and low-pressure regions toward the blade edges during operation. This shift can be attributed to centrifugal effects and flow acceleration around the blade geometry, phenomena that are well-documented in rotating hydrodynamic systems. Furthermore, as water continuously flows through the ASHT, a localized low-pressure zone forms at the trailing edge of the pressure side. This occurs due to the acceleration of water as it passes over the edge, leading to increased velocity and a corresponding drop in pressure, as described by Bernoulli's principle. This localized low-pressure zone contributes to the overall pressure gradient across the blade, thereby enhancing the turbine's torque generation capability. The outer sections of the blades, particularly near the leading edge, exhibit a significant pressure difference, indicating higher hydrodynamic loading in these regions. This observation is consistent with the expected behavior, where the leading edge experiences the initial impact of the incoming flow, resulting in pronounced pressure variations. The non-uniform pressure profiles across different ASHT configurations further underscore the influence of blade geometry on hydrodynamic performance. Specifically, configurations with variable blade angles, such as 30-45-60, 45-60-75, and 60-75-90, demonstrate more pronounced pressure differences compared to fixed-angle designs. These larger pressure differentials correlate with higher C_P, suggesting that variable blade angles optimize energy extraction by enhancing flow interaction and pressure gradients. The observed pressure profiles can be elucidated by the interplay between blade geometry and flow dynamics. Larger blade angles and variable configurations increase the effective surface area exposed to the incoming flow, thereby amplifying pressure differentials and improving energy capture.

4.2. Self starting performance

The starting torque is a crucial performance metric for hydrokinetic turbines, as it determines their ability to initiate rotation under low-flow conditions, which are commonly encountered in tidal and river environments. Fig. 8 illustrates a comparison of the starting torque coefficients ($C_{M,s}$) for nine ASHTs alongside three other hydrokinetic turbines (Zhang et al., 2023; Song et al., 2019): a Savonius turbine, a Propeller type turbine, and a traditional HAHT, all tested at a flow speed of 0.5 m/s. The results indicate significant variations in $C_{M,s}$ among the different ASHT configurations, with the 15-30-45° configuration achieving the highest $C_{M,s}$ of 0.311, while the 90-90-90° configuration shows the lowest $C_{M,s}$ of 0.133. This trend suggests that the starting torque of ASHTs decreases as the blade angle increases, a phenomenon that can be attributed to the interaction between blade geometry and hydrodynamic forces. The impact of blade angle on starting torque is fundamentally linked to the flow characteristics around the turbine. ASHTs with smaller blade angles experience less flow resistance, allowing water to pass through the turbine more efficiently. When water strikes the blades, the resulting force can be decomposed into tangential and radial components. For ASHTs with smaller blade angles, the tangential component represents a larger proportion of the total force, leading to greater torque generation and, consequently, higher starting torque. This behavior is consistent with the principles of fluid dynamics, where blade geometry directly influences the distribution of hydrodynamic forces and the efficiency of energy conversion. Moreover, ASHTs with variable blade angle configurations typically exhibit higher starting torques compared to fixed-angle designs. This is likely due to the adaptive nature of variable-angle blades, which optimize flow interaction and force distribution across a range of operating conditions. In contrast, fixed-angle configurations are less adaptable, resulting in suboptimal force distribution and diminished starting torque. When compared to other hydrokinetic turbines, ASHTs demonstrate competitive starting torque performance. The Savonius turbine, known for its strong self-starting capability as a vertical axis turbine, shows a $C_{M,s}$ comparable to ASHTs with moderate blade angles. This similarity highlights the effectiveness of ASHTs in low-flow conditions, despite their fundamentally different design. Conversely, propeller-type horizontal axis turbines, while exhibiting relatively good self-starting capabilities among traditional horizontal axis designs, still fall short of ASHTs in terms of $C_{M,s}$. Traditional three-blade horizontal axis turbines,

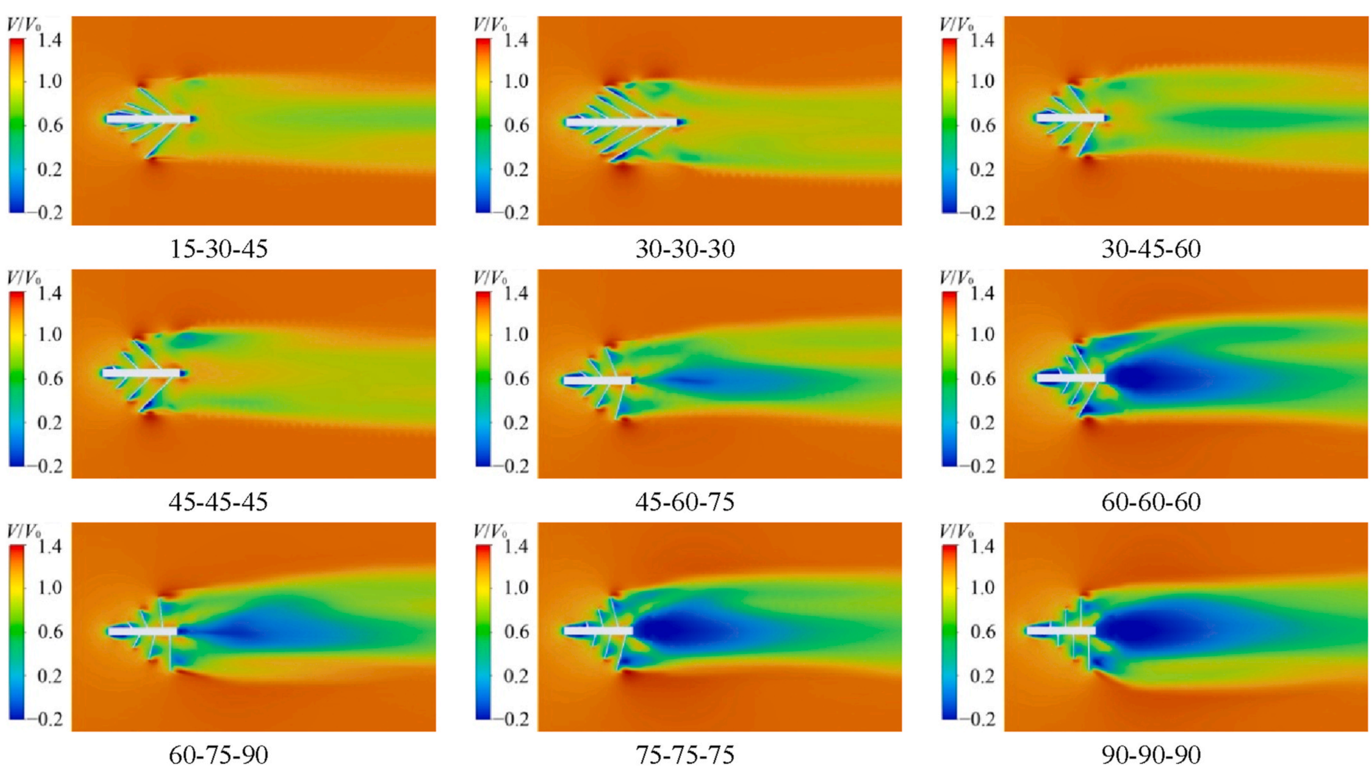

Fig. 9. Velocity contours of the ASHTs in axial flow ($TSR = 1.5$).

optimized for high-flow conditions, display extremely low $C_{M,s}$ under low-flow scenarios, rendering them ineffective for self-starting in such environments. The superior starting torque performance of ASHTs can be attributed to their unique helical blade geometry, which enhances flow interaction and torque generation even at low Reynolds numbers. At a Reynolds number of 1.2×10^5, ASHTs maintain a $C_{M,s}$ range of approximately 0.15–0.3, underscoring their suitability for low-speed flows.

4.3. Velocity contours

As water approaches the ASHT, the helical design of the blades facilitates rapid flow movement across their surfaces, generating a significant wake that has a diameter larger than that of the turbine itself. This wake is characterized by a reduction in flow velocity behind the ASHT, which reflects the conversion of kinetic energy into angular momentum. Fig. 9 illustrates the velocity contours for the nine ASHT configurations operating at a *TSR* of 1.5. The analysis reveals that the region near the blade tips exhibits the highest flow velocity, while the lowest velocity occurs near the hub, resulting in considerable turbulence in this area. These variations in velocity can be attributed to two primary factors: the rotational motion of the rotor and the wake generated by the hub. The flow dynamics around the ASHT are governed by the interplay between pressure gradients and blade geometry. High-pressure flow, aligned with the incoming water current, is directed outward toward the blade tips, while the flow on the suction side of the blades is drawn inward. This pressure differential drives the movement of water from high-pressure to low-pressure regions, as described by fundamental principles of fluid dynamics. When these opposing flows converge at the blade tips, they create a swirling motion that leads to the formation of tip vortices. These vortices are a common feature in HAHTs and contribute to the overall energy dissipation in the wake region. The velocity contours also highlight significant variations among the nine ASHT configurations, particularly concerning blade angle. ASHTs with smaller blade angles allow for more efficient flow over the blades, minimizing flow obstruction and reducing turbulence. In contrast, ASHTs with larger blade angles, such as the 90-90-90 configuration, exhibit higher levels of turbulence and more pronounced hub vortices. This is due to the increased flow obstruction caused by larger blade angles, which disrupts the smooth passage of water and amplifies recirculation effects. For instance, the 90-90-90 ASHT demonstrates a substantially larger low-velocity region and a more prominent hub recirculation zone compared to configurations with smaller blade angles.

4.4. Energy loss

To determine the entropy production rate (EPR), it suffices to consider the effective viscosity alongside the average velocity gradient, as shown in Eqs. (8) and (9). This theoretical foundation allows for the use of a steady-state solver to calculate the EPR. The EPR can be derived through a volume integral, as outlined in Eqs. (11) and (12). The volume integral method provides a mathematical framework for integrating relevant physical quantities over the entire computational domain, facilitating a comprehensive and accurate calculation of the EPR.

Fig. 10 illustrates the total entropy production for the nine ASHTs as the *TSR* varies. The entropy production curves for these configurations generally display a pattern of initial decline followed by an increase as *TSR* rises. At low *TSR* values, flow separation and stalling are prevalent, resulting in the mixing of free-stream flow with reverse flow around the blades. This mixing leads to significant energy losses due to increased turbulence and inefficient energy transfer. As *TSR* increases, flow separation is mitigated, which reduces energy losses and enhances turbine efficiency. However, at higher *TSR* values, the interaction between the blades and the incoming flow intensifies, leading to a substantial exchange of momentum. This interaction increases the relative velocity of the flow, generating turbulence and vortices that exacerbate energy

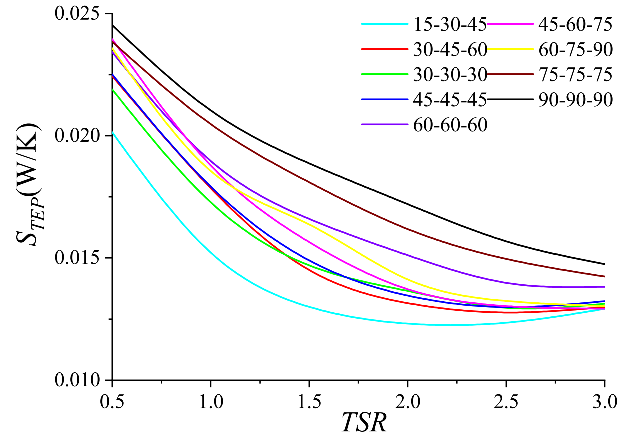

Fig. 10. Total Entropy production versus *TSR* curves for the ASHTs in axial flow.

losses. These observations align with established principles of fluid dynamics, where energy dissipation is closely linked to flow separation, turbulence, and vortex formation. The total entropy production is also influenced by blade angle, with configurations featuring larger blade angles consistently exhibiting higher entropy production. This trend can be attributed to the increased flow obstruction and higher pressure differentials associated with larger blade angles, which amplify turbulence and vortex generation. For instance, the 90-90-90 configuration, which has the largest blade angle, demonstrates the highest entropy production due to its pronounced flow blockage and enhanced vortex activity.

Fig. 11 depicts the entropy production rate (EPR) distribution for the nine ASHTs, providing further insight into the spatial characteristics of energy loss. The EPR is concentrated near the turbine and extends downstream, primarily due to the formation of tip and hub vortices. Tip vortices arise from the pressure difference across the blade surfaces, while hub vortices result from flow separation and recirculation behind the hub. These vortices contribute to high EPR regions near the turbine, with their effects propagating downstream along the main flow. In the far wake, the EPR diminishes as kinetic energy is gradually restored, leading to more uniform flow conditions. Configurations with larger blade angles, such as 60-75-90, 75-75-75, and 90-90-90, exhibit more pronounced EPR, particularly in the hub region. This is due to the high blockage effect of larger blade angles, which forces a greater volume of fluid through the central rotor region, intensifying hub vortices and energy losses. These hub vortices remain influential up to a distance of approximately $z = 5\mathrm{D}$, significantly impacting the wake structure. In contrast, tip vortices primarily affect the leading edge of the wake and have a comparatively smaller influence on energy loss. These observations underscore the critical role of blade angle in determining the distribution and magnitude of energy losses in ASHTs.

The energy loss coefficient (C_l) performs a quantitative analysis of energy loss, which is defined as follow: where, $0.5\rho A_c V_0^3$ is the input power at the inlet, and $\int_{A_e} f_{EPR} dA_e$ is the integral area of the EPR, which represents the local energy loss relative to the input energy.

$$C_l = \frac{\int_{A_e} f_{EPR} dA_e}{\frac{0.5\rho A_c V_0^3}{V_c T} A_e} \tag{14}$$

here, V_c indicates the volume of the computational domain, A_c denotes the inlet area of the computational domain and A_e represents the area of the integration region.

Fig. 12 presents the C_l values on the x-y plane from $z = 1\mathrm{D}$ to $z = 12\mathrm{D}$ for the nine ASHTs at TSR values of 0.5, 1.0, 1.5, and 2.0. The C_l values generally decrease with increasing distance downstream, reflecting the gradual recovery of kinetic energy in the wake. At lower *TSR* values, C_l is

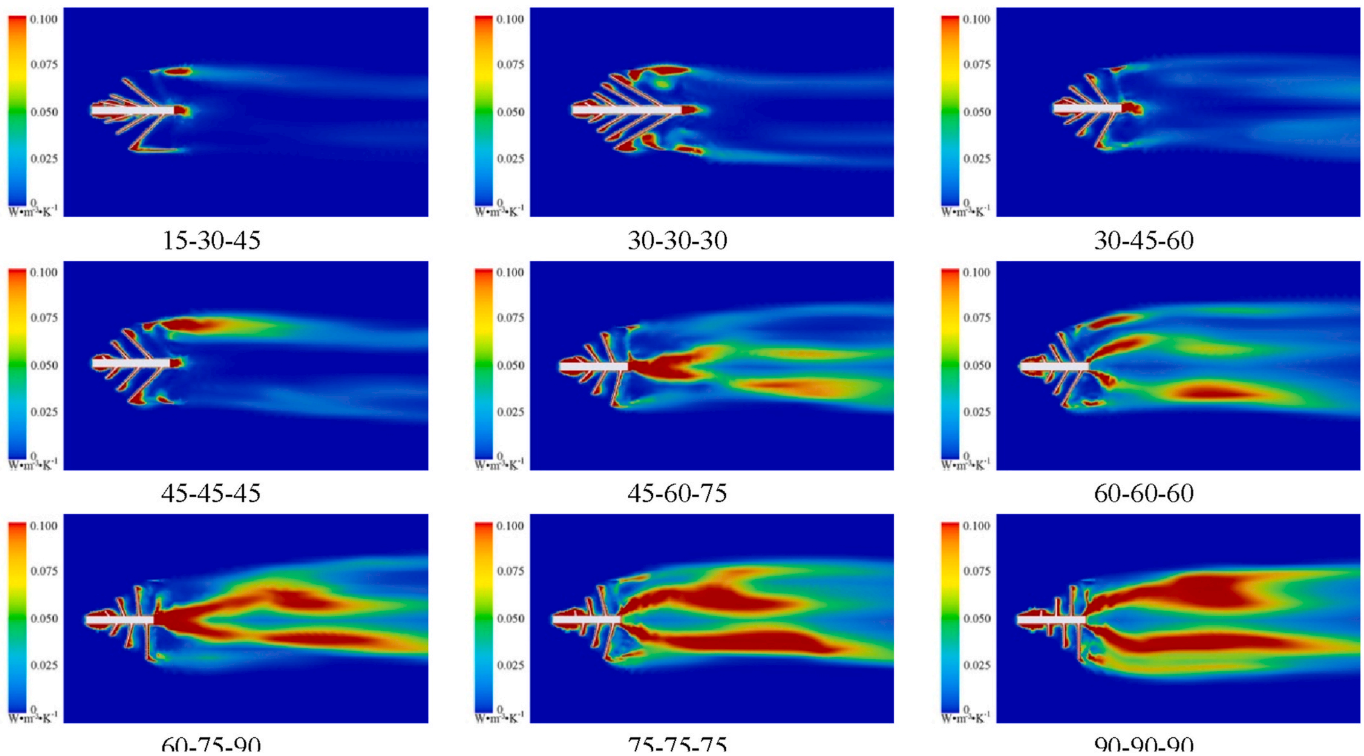

Fig. 11. Total entropy production rate distribution of the ASHTs in axial flow (TSR = 1.5).

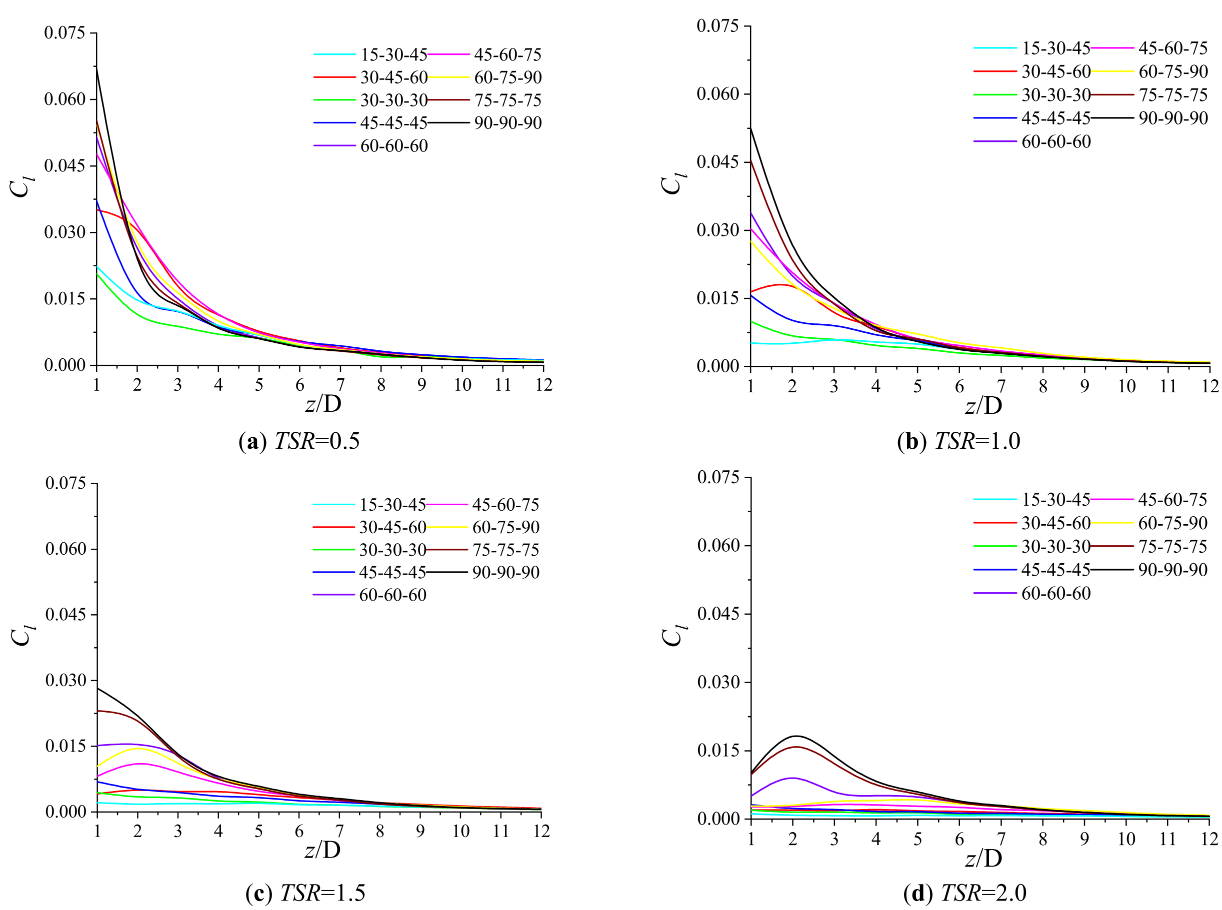

Fig. 12. Profiles of C_l for the ASHTs in axial flow.

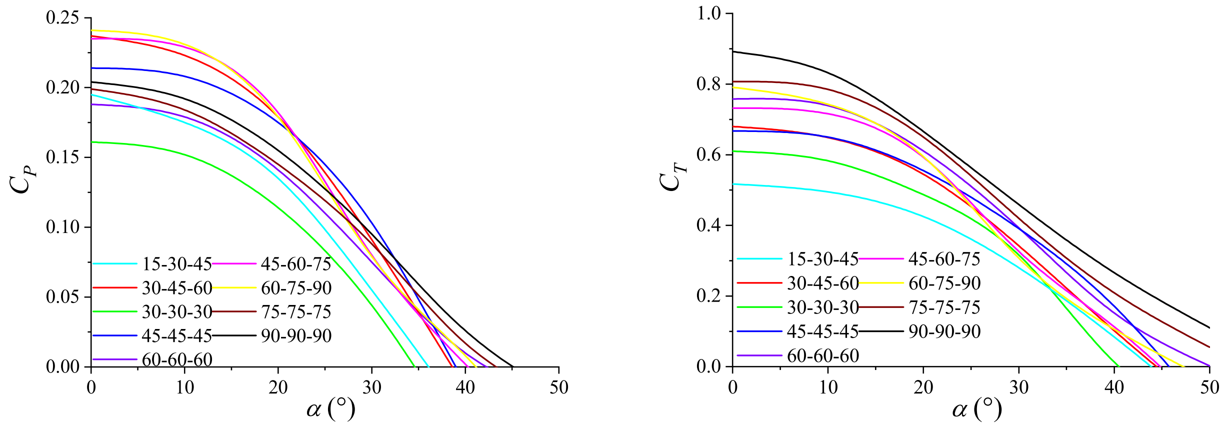

(**a**) C_P (**b**) C_T

Fig. 13. C_P and C_T versus α curves for the ASHTs in yawed flow.

significantly higher, consistent with the entropy production trends shown in Fig. 10. For example, the 90-90-90 configuration, which has the lowest power coefficient, exhibits a maximum C_l of 0.0605 at $z = 1$D under $TSR = 0.5$. Across all TSR conditions, C_l decreases to 0.02 in the wake between 8D and 9D, indicating the extent of energy loss and recovery. The C_l metric provides a quantitative measure of energy dissipation and kinetic energy recuperation in the wake, offering valuable insights into the nature and location of energy losses.

5. Results in yawed flow

5.1. Power, thrust and pressure

Fig. 13 illustrates the relationship between the C_P and C_T for the nine ASHTs at a TSR of 1.5, as the yaw angle (α) varies. At a yaw angle of 10°, the reductions in C_P and C_T across all ASHT configurations are minimal, indicating that small yaw angles have a negligible impact on turbine performance. However, as the yaw angle increases, the decline in C_P and C_T becomes more pronounced. For instance, the 60-75-90 ASHT shows reductions in C_P of −4.1%, −25.7%, −67.2%, −96.7%, and −129.5% at yaw angles of 10°, 20°, 30°, 40°, and 50°, respectively, compared to axial flow conditions. Similarly, C_T decreases by −2.5%, −19.4%, −48.2%, −79.9%, and −99.7% at the same yaw angles. These performance trends can be attributed to the hydrodynamic behavior of ASHTs under yawed flow conditions. As the yaw angle increases, the axial projected area of the ASHT decreases, which reduces the effective kinetic energy available for conversion by the turbine. This reduction in energy capture is further exacerbated by intensified flow separation at

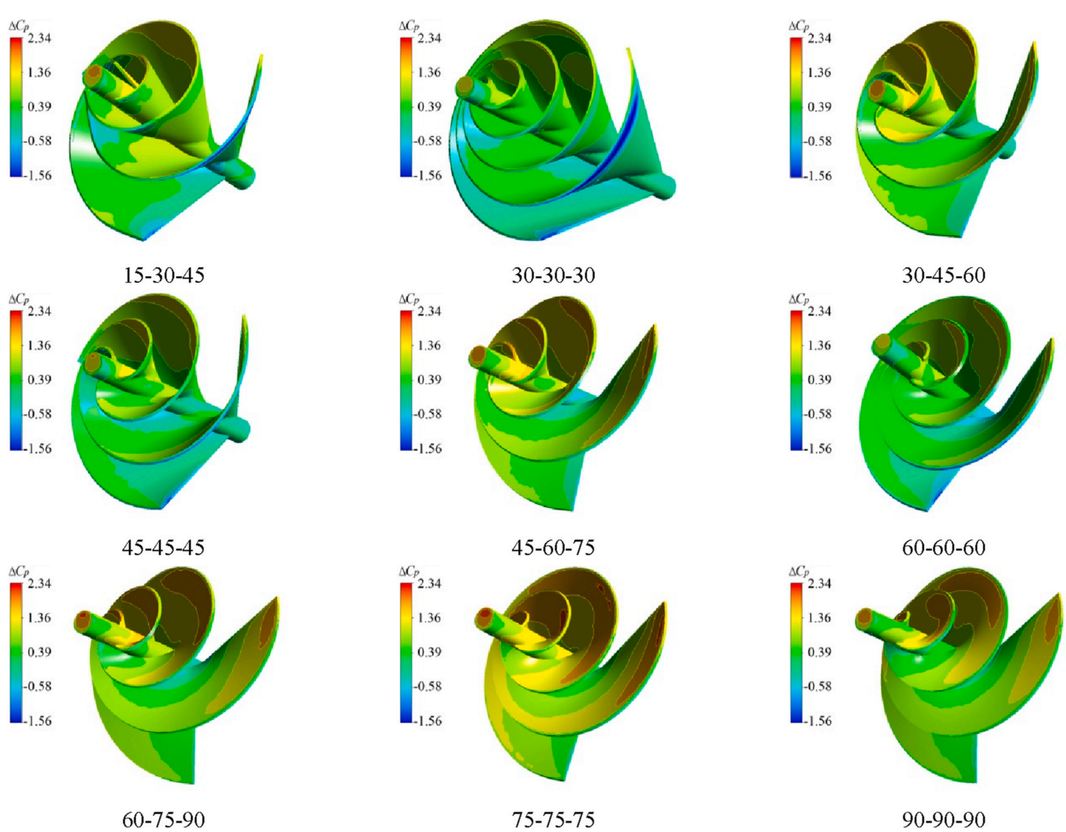

Fig. 14. Pressure coefficient ($\Delta C_p = \frac{p}{0.5\rho V_0^2}$) distribution on the ASHTs in yawed flow ($\alpha = 20°$).

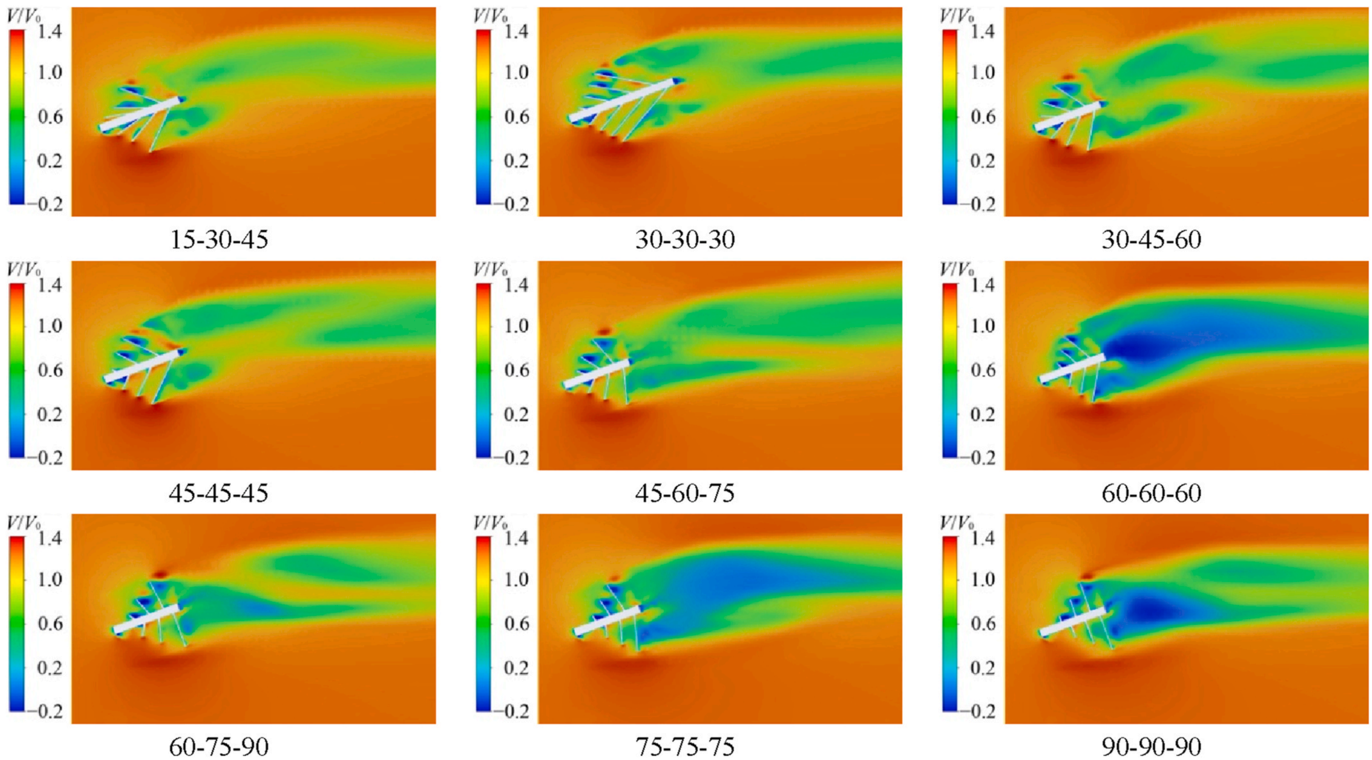

Fig. 15. Velocity contours of the ASHTs in yawed flow ($\alpha = 20^{\circ}$).

the front end of the elongated rotor shaft, leading to increased turbulence in the upstream flow. This turbulence disrupts the smooth interaction between the flow and the blades, resulting in inefficiencies in energy extraction, as illustrated in Fig. 15. Additionally, yawed flow alters the orientation of the incoming flow relative to the rotor, decomposing it into two components: a spanwise component and an axial component. Only the axial component contributes to the generation of thrust and torque, while the spanwise component primarily induces drag and secondary flow effects, further diminishing turbine efficiency. The impact of yaw angle on performance is also influenced by blade geometry. ASHTs with larger blade angles, such as the 90-90-90 configuration, exhibit a broader operating range of yaw angles and maintain positive C_P values even at $\alpha = 45^{\circ}$. This resilience can be attributed to the enhanced flow interaction and adaptability of larger blade angles under varying flow conditions. In contrast, fixed blade angle configurations, such as 30-30-30, 45-45-45, 60-60-60, and 75-75-75, demonstrate a wider range of effective yaw angles compared to their variable blade angle counterparts (e.g., 15-30-45, 30-45-60, 45-60-75, and 60-75-90). This suggests that fixed blade angles may offer greater stability and performance consistency under yawed flow conditions, albeit at the cost of reduced adaptability. These findings align with established principles of fluid dynamics and turbine aerodynamics, where yawed flow is known to reduce the effective energy capture area and induce complex flow phenomena such as flow separation and turbulence. The observed performance trends are consistent with studies on other HAHTs, which have shown that yawed flow significantly impacts energy extraction efficiency.

Fig. 14 illustrates the distribution of the pressure coefficient (ΔC_p) for the nine ASHTs operating at a yaw angle (α) of 20°. Similar to the dynamics observed under axial flow conditions, all ASHT configurations demonstrate increased pressure on the pressure side and decreased pressure on the suction side when subjected to yawed flow. However, the introduction of yawed flow results in significant asymmetries in the pressure distribution across the blades. In axial flow, the ΔC_p distribution remains consistent in the circumferential direction, indicating a uniform interaction between the flow and the blades. In contrast, yawed flow generates a region of elevated pressure on the deflected side of the rotor, which alters the flow dynamics and reduces the overall pressure differential across the blades. This phenomenon occurs because yawed flow allows the incoming water to bypass the blade tip more easily, reaching the suction side with less resistance. Consequently, the pressure differential between the pressure and suction sides diminishes, leading to a notable decline in both the C_P and C_T. This reduction in performance aligns with established principles of fluid dynamics, where yawed flow decreases the effective energy capture area and disrupts the optimal flow interaction necessary for efficient energy extraction. The observed changes in pressure also correspond with findings from studies on HAHTs, which have shown that yawed flow induces similar asymmetries and performance degradation. Moreover, prolonged operation under yawed flow conditions can exacerbate the pressure differential across the blades, resulting in increased dynamic stress on the turbine structure. This elevated dynamic stress can accelerate fatigue and structural wear, potentially compromising the long-term durability and

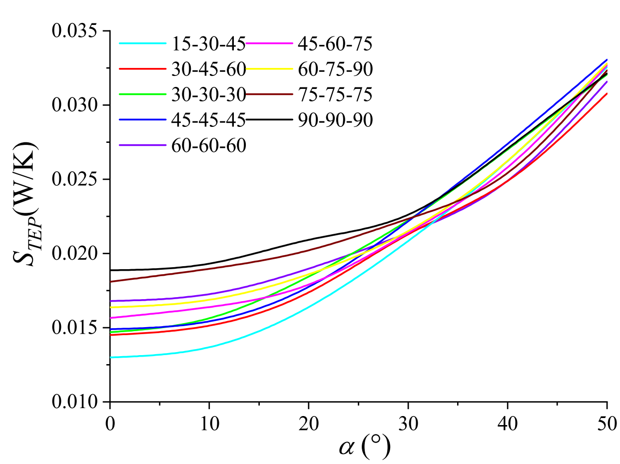

Fig. 16. Total Entropy production versus α curves for the ASHTs in yawed flow.

reliability of the turbine.

5.2. Velocity contours

Fig. 15 illustrates the velocity contours for the nine ASHTs operating at a yaw angle (α) of 20° and a *TSR* of 1.5. The analysis indicates that all ASHT configurations experience unsteady flow separation under yawed conditions, resulting in a wake that is significantly more turbulent compared to axial flow conditions. When water interacts with the rotor, a high-speed region forms near the blade tips; however, this velocity diminishes as the flow progresses downstream. Concurrently, a low-speed region develops behind the hub due to flow obstruction, disrupting the downstream flow field. This behavior aligns with the energy conversion process, where the kinetic energy of the incoming flow is transformed into mechanical energy by the blades, leading to a substantial reduction in the axial velocity component immediately downstream of the turbine. Further downstream, the flow gradually recovers its velocity as kinetic energy is replenished in the wake region. Under yawed conditions, the wake of the ASHT undergoes both displacement and distortion, with the yaw angle (α) playing a critical role in determining the direction and magnitude of wake deflection. This result in a significant alteration of the wake shape, which is displaced to one side, creating a complex and asymmetric flow field downstream. This complexity arises because the incoming flow separates into axial and tangential components when interacting with the yawed rotor. The axial component, primarily responsible for energy extraction, is diminished, while the tangential component induces secondary flow effects, further complicating the wake structure. This asymmetric flow pattern and the reduced axial momentum in the wake are key factors contributing to the performance degradation observed under yawed conditions. A notable distinction between ASHTs and HAHTs is the behavior of the wake width under yawed flow. While the wake of a HAHT typically narrows as the yaw angle increases, the wake width of an ASHT remains relatively unchanged. This difference can be attributed to the greater axial length of ASHTs, which ensures that the projected area facing the incoming flow remains largely consistent even under yawed conditions. This characteristic of ASHTs mitigates the reduction in wake width, but it also contributes to the persistence of turbulence and flow complexity in the wake.

5.3. Energy loss

Fig. 16 illustrates the total entropy production for the nine ASHTs at various yaw angles (α). The results indicate a consistent increase in total entropy production as the yaw angle increases. For example, the 60-75-90 configuration shows minimal changes in entropy production at yaw angles of $\alpha = 0°$ and 10°. However, a significant increase in entropy production is observed when the yaw angle rises to 20° and beyond. Specifically, compared to $\alpha = 0°$, the entropy production at $\alpha = 20°$, 30°, 40°, and 50° increases by factors of 1.14, 1.31, 1.60, and 2.00, respectively. This trend can be attributed to the enhanced turbulence intensity and velocity gradient induced by larger yaw angles, which amplify energy dissipation and entropy generation. These observations are consistent with the principles of fluid dynamics, where increased flow complexity and turbulence lead to higher entropy production. At smaller yaw angles ($\alpha < 20°$), the ranking of total entropy production among the nine ASHT configurations remains consistent with that observed under axial flow conditions. Configurations featuring larger blade angles generally produce higher entropy due to greater flow obstruction and pressure differentials, which intensify turbulence and energy losses. However, as the yaw angle exceeds 40°, this trend is disrupted. For instance, the 45-45-45 configuration exhibits higher entropy production than configurations with larger blade angles, such as 60-60-60 and 75-75-75. This shift suggests that, at high yaw angles, factors such as flow separation and vortex formation become more significant in determining entropy production than blade angle alone.

Fig. 17 depicts the entropy production rate (EPR) distribution for the nine ASHTs at $\alpha = 20°$. The figure reveals a localized area of elevated entropy rate near the upper half of one side of the blades, with the tip region experiencing higher losses compared to axial flow conditions.

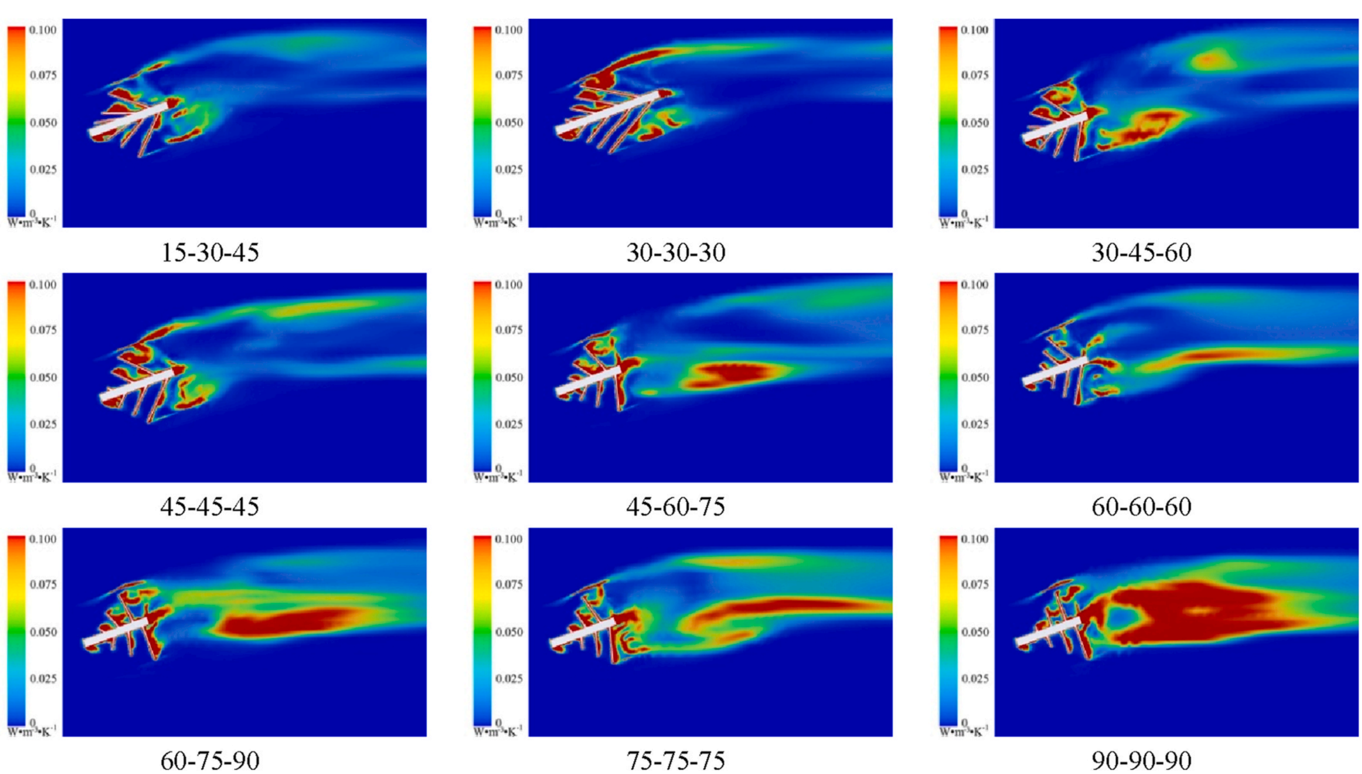

Fig. 17. Total entropy production rate distribution of the ASHTs in yawed flow ($\alpha = 20°$).

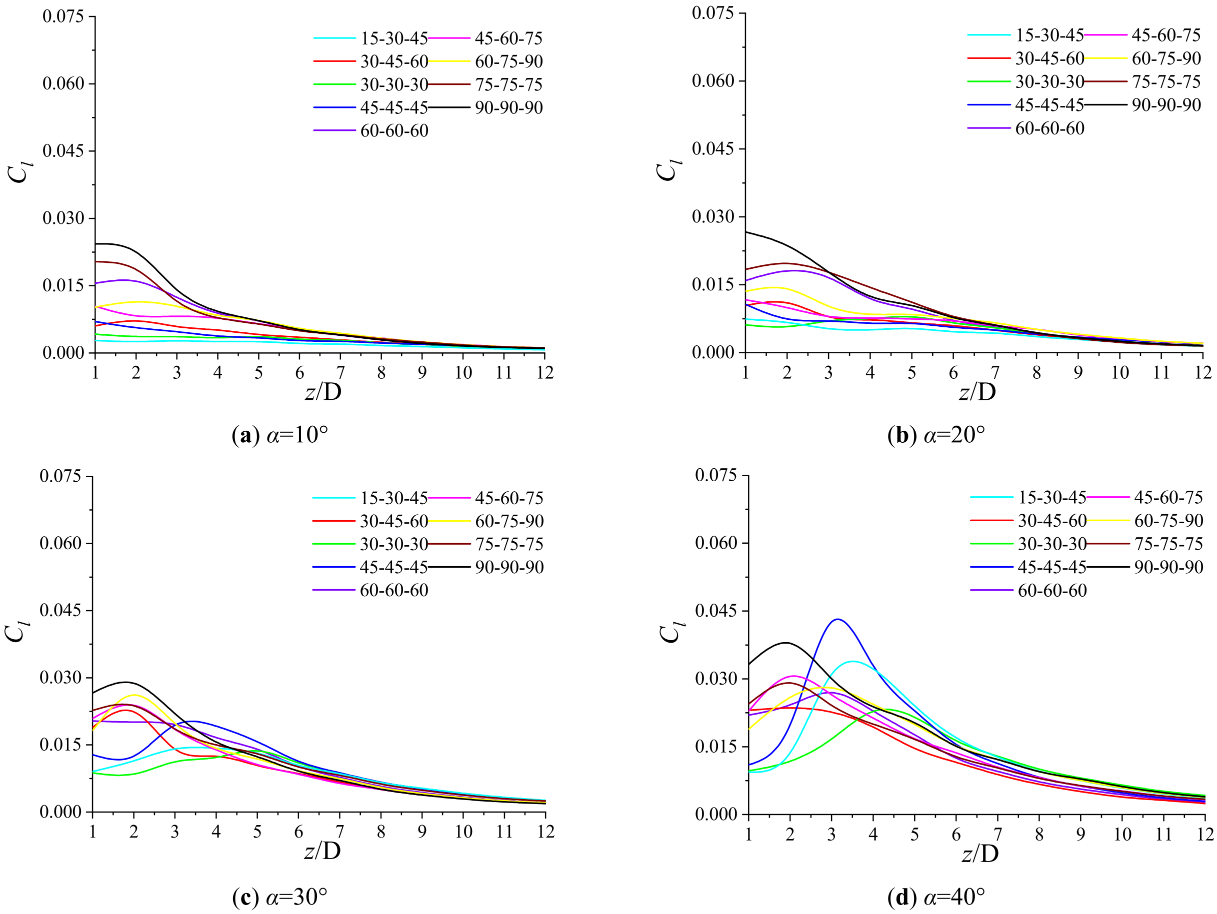

Fig. 18. Profiles of C_l for the ASHTs in yawed flow.

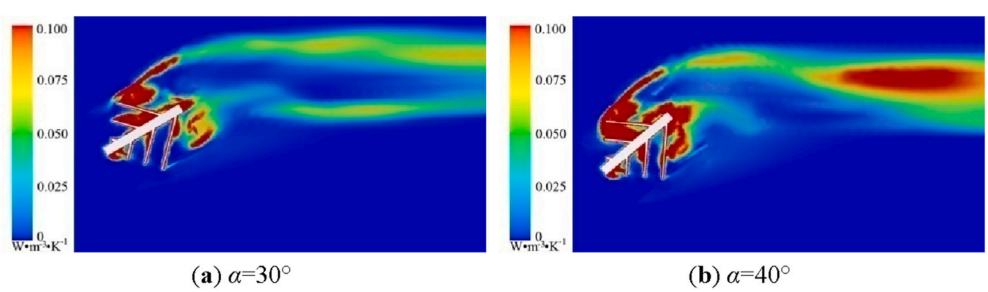

Fig. 19. Total entropy production rate distribution of the 45-45-45 configuration at $\alpha = 30^\circ$ and 40°.

This phenomenon is a direct consequence of yawed flow, where flow separation initiates from the blade edges on the deflected pressure side, generating significant vortices that envelop the blade surface. A comparison of Fig. 17 with Fig. 11 (axial flow conditions) further highlights the increased EPR within the wake under yawed flow, which adopts increasingly complex and asymmetric shapes as it propagates downstream. The majority of entropy production occurs near the tip and hub of the ASHT, primarily due to extensive flow separation and vortex generation in these regions. These vortices are the main contributors to overall entropy production, as they induce energy dissipation and disrupt the flow field.

Fig. 18 presents the C_l values on the x-y plane from $z = 1D$ to $z = 12D$ for the nine ASHTs at yaw angles of 10°, 20°, 30°, and 40°. At $\alpha = 10^\circ$ and 20°, the C_l distribution follows a consistent trend, gradually decreasing with increasing downstream distance. However, at $\alpha = 30^\circ$ and 40°, the C_l pattern shifts, showing an initial rise followed by a decline. Notably, the 45-45-45 configuration exhibits a peak in C_l at $\alpha =$ 40°, indicating a localized increase in energy loss and flow complexity. This behavior is further elucidated in Fig. 19, which illustrates the EPR for the 45-45-45 configuration at $\alpha = 30^\circ$ and 40°. At $\alpha = 40^\circ$, the blade on the deflected side of the 45-45-45 configuration becomes nearly perpendicular to the incoming flow. According to the principle of least resistance, water flows around one side of the ASHT, leading to flow separation and the formation of extensive separation vortices. These vortices create regions of high local entropy production, contributing to the overall increase in energy dissipation.

6. Discuss

While this study primarily examines the performance characteristics of the ASHT under low-flow conditions, it is crucial to assess the impact of the Reynolds number (Re) on its performance. The 30-45-60 configuration serves as a case study to investigate this relationship. Fig. 20 illustrates how the C_P and C_T vary as a function of the TSR for the 30-45-

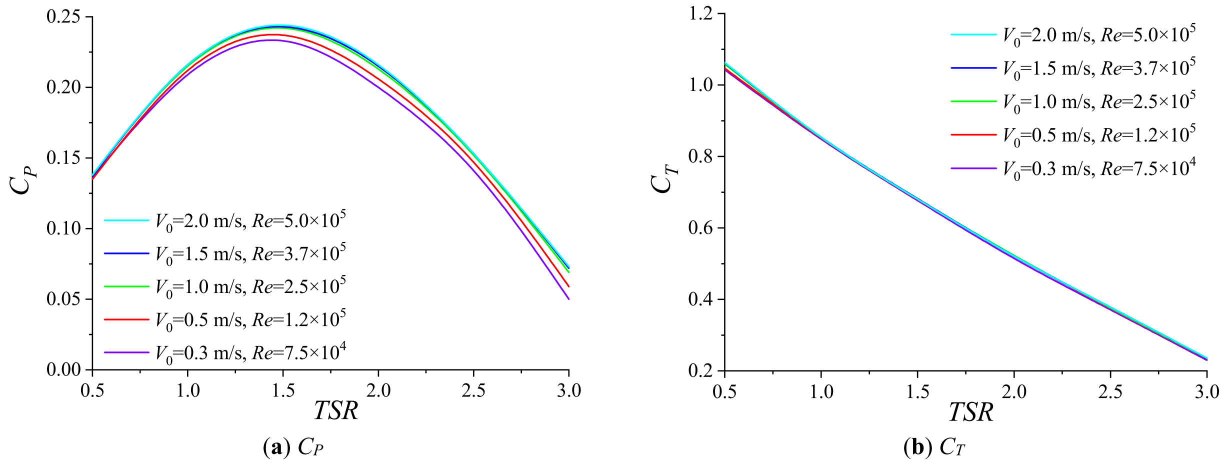

Fig. 20. C_P and C_T versus *TSR* curves for the 30-45-60 at different Reynolds numbers.

60 configuration across different Reynolds numbers. The results indicate that as the *Re* increases—corresponding to flow velocities (V_0) rising from 0.3 m/s to 2.0 m/s, which translates to *Re* values from 7.5 × 10^4 to 5.0 × 10^5—there is a significant improvement in C_P. For example, when the flow velocity is 0.3 m/s (Re = 7.5 × 10^4), the peak C_P is approximately 0.233. In contrast, at Re = 5.0 × 10^5, the peak C_P increases to about 0.245, reflecting an enhancement of roughly 5.2%. This trend is consistent with findings from Bourhis et al. (2023), which suggest that higher Reynolds numbers improve the peak C_P by reducing flow separation and enhancing flow attachment to the blade surfaces, thereby increasing energy extraction efficiency. The C_P-*TSR* curves further reveal that higher Reynolds numbers lead to broader operational ranges and a gradual shift of the optimal *TSR* to higher values. For instance, at Re = 7.5 × 10^4, the optimal *TSR* is approximately 1.4, whereas at Re = 5.0 × 10^5, it rises to about 1.6. This shift can be attributed to improved flow dynamics at higher Reynolds numbers, where reduced viscous effects and enhanced momentum transfer enable the turbine to operate efficiently at elevated *TSR* values. These observations align with the mechanisms described by Bourhis et al. (2023), which emphasize the role of Reynolds number in optimizing turbine performance. Notably, when the Reynolds number reaches 3.7 × 10^5, the C_P curve nearly coincides with that at Re = 5.0 × 10^5, suggesting that the influence of *Re* on the peak C_P becomes less pronounced beyond this threshold. This indicates that the primary effect of *Re* on ASHT's performance is most significant at lower to moderate Reynolds numbers ($Re \leq 3.7 \times 10^5$), where viscous effects and flow separation are more dominant. Similarly, the effect of Reynolds number on the C_T mirrors its impact on C_P. As *Re* increases, C_T also experiences an enhancement, reflecting improved flow interaction and momentum transfer at higher flow velocities. This trend further underscores the importance of Reynolds number in determining both the energy extraction efficiency and the hydrodynamic loading of the ASHT. In summary, the increase in flow velocity and Reynolds number enhances flow attachment to the ASHT blades, improving both C_P and C_T while broadening the operational range of *TSR*. However, the overall performance improvement is relatively modest, particularly at higher Reynolds numbers ($Re > 3.7 \times 10^5$), where the influence of *Re* diminishes.

On the other hand, although the theory of entropy production is a powerful tool for diagnosing energy losses in turbines, it does not constitute a complete theory of energy dissipation. To the best of our knowledge, there is currently no fully satisfactory general theory regarding energy losses in open flow turbines (such as wind turbines or hydrokinetic turbines). In our current research, the analysis of energy losses in ASHT has not yet covered all aspects and has certain limitations. The entropy production theory focuses on irreversible losses caused by viscosity and turbulence, but it does not account for all forms of energy loss. For instance, at low *TSR*, additional kinetic energy losses occur in the wake due to the higher circumferential velocity. These losses are not related to entropy production, as evidenced by the values of C_l in Fig. 12, which are relatively small compared to C_P. Moreover, some researchers also have analyzed the energy loss behavior of turbines using entropy production theory while neglecting the effects of heat conduction and radiation under the assumption of constant environmental temperature. For example, Shen et al. (2024) conducted an analysis of energy losses in double Darrieus vertical axis wind turbine and found that as the pitch angle of the outer rotor increases, both total entropy production and turbulent entropy production gradually decrease. In most azimuth angles, an increase in the pitch angle of the inner rotor leads to a gradual increase in total entropy production. Similarly, Zang et al. (2022) analyzed the energy losses in ducted hydrokinetic turbines and discovered that high entropy production areas are located at the duct entrance, blade tips, and behind the hub, as well as at the diffuser exit. They noted that the entropy production rate in the near-wake region deflects towards the free surface and the bottom of the tank. However, the aforementioned studies do not explain all forms of energy loss, particularly those related to the global flow and wake recovery of turbines at different *TSR*s. Nevertheless, this does not preclude the use of entropy production theory as a supplementary perspective. By quantifying irreversible losses associated with fluid viscosity and turbulent dissipation processes, it aids in identifying the specific locations and mechanisms of flow losses within the flow field. In our research, we successfully employed the theory of entropy production to quantify and locate these losses, particularly in the wake region and near the blade tips and hub, where significant vortices and flow separation phenomena occur. This approach enables us to identify specific areas and mechanisms of energy dissipation that traditional analytical methods cannot match.

7. Conclusions

This comprehensive study explores the hydrodynamics and energy loss characteristics of nine ASHTs with varying blade angles, assessing their performance under both axial and yawed flow conditions. By analyzing key parameters such as power coefficient, thrust coefficient, pressure coefficient, velocity contours, total entropy production, and energy loss coefficient, this research provides critical insights into optimizing ASHT's performance.

The findings indicate that ASHTs with larger blade angles exhibit a wider operating range of *TSR*s and achieve peak performance at higher *TSR*s, while also generating greater thrust coefficients. This suggests that ASHTs with larger blade angles may be more adaptable due to their ability to operate efficiently across a broader range of conditions.

However, the increased thrust associated with larger blade angles also implies higher structural loads, necessitating robust design considerations to ensure the turbine's longevity. Furthermore, variable-angle configurations demonstrate higher peak power coefficients and lower thrust coefficients compared to fixed blade angle configurations. This highlights their potential for optimizing energy extraction while minimizing structural stress, making them particularly suitable for dynamic flow environments.

The study also emphasizes the significance of wake dynamics and energy loss mechanisms. Larger blade angle configurations create a more extensive low-velocity region behind the turbine, accompanied by a prominent hub recirculation zone. Energy loss in the wake is primarily driven by tip and hub vortices, with hub vortices being the dominant contributors to elevated EPR in configurations with larger blade angles. Under yawed flow conditions, increasing yaw angles lead to significant reductions in C_P and C_T, altered wake structures, and increased total entropy production. The pressure distribution across the turbine is modified, reducing the pressure differential between the two sides and further diminishing performance. While variable-angle configurations are efficient, they exhibit a narrower operating range of yaw angles compared to fixed blade angle configurations, indicating a trade-off between adaptability and performance under yawed flows.

Additionally, the study highlights the influence of the Reynolds number on ASHT performance. As the Reynolds number increases, both the power coefficient and thrust coefficient improve, and the operational range of *TSR* broadens. However, at higher Reynolds numbers ($Re > 3.7 \times 10^5$), the performance gains become less pronounced, suggesting that operators must carefully balance the cost-benefit of deploying turbines in high-velocity flow areas. The energy loss coefficient emerges as a valuable metric for quantifying energy loss and kinetic energy recovery in the wake, underscoring the importance of optimizing ASHT configurations to enhance energy efficiency and profitability in ocean current power generation.

In summary, the study's findings translate into actionable recommendations for ASHT design and operation: (1) In environments with variable flow speeds, ASHTs with larger blade angles should be prioritized due to their broader operational range, but structural reinforcements are necessary to accommodate increased thrust. (2) Incorporating variable blade angle configurations can optimize energy extraction and reduce structural stress. (3) Designers should aim to balance blade angle and flow dynamics to minimize energy losses, potentially through hybrid configurations or advanced flow control techniques. (4) Designers should consider the Reynolds number in site selection, targeting areas with optimal flow velocities to maximize efficiency. By implementing these recommendations, the efficiency, reliability, and profitability of ASHTs in tidal energy applications can be significantly enhanced.

CRediT authorship contribution statement

Ke Song: Writing – original draft, Software, Methodology, Funding acquisition, Conceptualization. **Hui-Ting Huan:** Validation, Software. **Liu-Chuang Wei:** Writing – review & editing. **Chun-Xia Liu:** Writing – review & editing, Supervision.

Data availability

No data was used for the research described in the article.

Declaration of competing interest

The authors declare that they have no known competing financial interests or personal relationships that could have appeared to influence the work reported in this paper.

Acknowledgement

This work was supported by the Yunnan Fundamental Research Project (2025 Research on the Correlation Mechanism between Spatiotemporal Evolution of Vortices and Energy Harvesting Characteristics in Spiral Hydrokinetic Turbine), the Xingdian Talent Support Program of Yunnan Province (grant no. XDYC-QNRC-2023-0159), and the Key Laboratory of Yunnan Advanced Equipment Intelligent Manufacturing Technology (grant no. KLYAEIMTY2022001). The authors are grateful for this financial support.

References

Al-Dabbagh, M.A., Yuce, M.I., 2019. Numerical evaluation of helical hydrokinetic turbines with different solidities under different flow conditions. Int. J. Environ. Sci. Technol. 16, 4001–4012.

Allmark, M., Ellis, R., Lloyd, C., Ordonez-Sanchez, S., Johannesen, K., Byrne, C., Mason-Jones, A., 2020. The development, design and characterisation of a scale model Horizontal Axis Tidal Turbine for dynamic load quantification. Renew. Energy 156, 913–930.

Badawy, Y.E., Nawar, M.A., Attai, Y.A., Mohamed, M.H., 2023. Co-enhancements of several design parameters of an archimedes spiral turbine for hydrokinetic energy conversion. Energy, 126715.

Bakırcı, M., Yılmaz, S., 2018. Theoretical and computational investigations of the optimal tip-speed ratio of horizontal-axis wind turbines. Eng. Sci. Technol. Int. J. 21 (6), 1128–1142.

Bourhis, M., Pereira, M., Ravelet, F., 2023. Experimental investigation of the effects of the Reynolds number on the performance and near wake of a wind turbine. Renew. Energy 209, 63–70.

Gao, R.J., Chen, J.H., Zhang, J.J., Zhou, S.Y., Xu, H.F., Wu, J.D., Qian, X.H., 2020. Hydrodynamic study on energy capturing performance of horizontal axis blades under sub-low speed tidal current. China Ocean Eng. 34 (3), 374–386.

Ghisu, T., Cambuli, F., Puddu, P., Mandas, N., Seshadri, P., Parks, G., 2018. Numerical evaluation of entropy generation in isolated airfoils and wells turbines. Meccanica 53, 3437–3456.

Guo, T., Wang, H.Y., 2023. Analysis of hydrodynamic characteristics and loss mechanism of hydrofoil under high Reynolds number. Ocean Eng. 287, 115892.

Herwig, H., Kock, F., 2007. Direct and indirect methods of calculating entropy generation rates in turbulent convective heat transfer problems. Heat Mass Tran. 43 (3), 207–215.

Kamal, A.M., Nawar, M.A., Attai, Y.A., Mohamed, M.H., 2022. Blade design effect on archimedes spiral wind turbine performance: experimental and numerical evaluations. Energy 250, 123892.

Kock, F., Herwig, H., 2004. Local entropy production in turbulent shear flows: a high-Reynolds number model with wall functions. Int. J. Heat Mass Tran. 47 (10), 2205–2215.

Laws, N.D., Epps, B.P., 2016. Hydrokinetic energy conversion: Technology, research, and outlook. Renew. Sustain. Energy Rev. 57, 1245–1259.

Lawson, M.J., Li, Y., Sale, D.C., 2011. Development and verification of a computational fluid dynamics model of a horizontal-axis tidal current turbine. Int. Conf. Offshore Mech. Arctic Eng. 44373, 711–720.

Li, D., Wang, H., Qin, Y., Han, L., Wei, X., Qin, D., 2017. Entropy production analysis of hysteresis characteristic of a pump-turbine model. Energy Convers. Manag. 149, 175–191.

Li, L., Lin, J., Wu, N., Xie, S., Meng, C., Zheng, Y., Zhao, Y., 2022. Review and outlook on the international renewable energy development. Energy Built Environ. 3 (2), 139–157.

Menter, F.R., 1994. Two-equation eddy-viscosity turbulence models for engineering applications. AIAA J. 32 (8), 1598–1605.

Monatrakul, W., Senawong, K., Sritram, P., Suntivarakorn, R., 2023. A comparison study of hydro-compact generators with horizontal spiral turbines (HSTs) and a three-blade turbine used in irrigation canals. Energies 16 (5), 2267.

Monatrakul, W., Suntivarakorn, R., 2017. Effect of blade angle on turbine efficiency of a spiral horizontal Axis hydro turbine. Energy Proc. 138, 811–816.

Moshfeghi, M., Shams, S., Hur, N., 2017. Aerodynamic performance enhancement analysis of horizontal axis wind turbines using a passive flow control method via split blade. J. Wind Eng. Ind. Aerod. 167, 148–159.

Moshfeghi, M., Song, Y.J., Xie, Y.H., 2012. Effects of near-wall grid spacing on SST-K-ω model using NREL Phase VI horizontal axis wind turbine. J. Wind Eng. Ind. Aerod. 107, 94–105.

Nazeryan, M., Lakzian, E., 2018. Detailed entropy generation analysis of a Wells turbine using the variation of the blade thickness. Energy 143, 385–405.

Nunes, M.M., Junior, A.C.B., Oliveira, T.F., 2020. Systematic review of diffuser-augmented horizontal-axis turbines. Renew. Sustain. Energy Rev. 133, 110075.

Olabi, A.G., Abdelkareem, M.A., 2022. Renewable energy and climate change. Renew. Sustain. Energy Rev. 158, 112111.

Satrio, D., Utama, I.K.A.P., 2021. Experimental investigation into the improvement of self-starting capability of vertical-axis tidal current turbine. Energy Rep. 7, 4587–4594.

Shen, Z., Gong, S., Lu, H., Guo, W., Chen, W., 2024. Investigation of the effect of pitch angle of double Darrieus vertical axis wind turbine based on aerodynamic performance and entropy production theory. Ocean Eng. 311, 118930.

Song, K., Huan, H.T., Wei, L.C., Liu, C.X., 2024. A comparative study of hydrodynamic performance between ducted and non-ducted Archimedes spiral hydrokinetic turbines. Ocean Eng. 306, 118087.
Song, K., Kang, Y., 2022a. Fluid-structure interactions analysis of a drag-type horizontal Axis hydraulic turbine. J. Phys. Conf. 2404, 012001.
Song, K., Kang, Y., 2022b. A numerical performance analysis of a rim-driven turbine in real flow conditions. J. Mar. Sci. Eng. 10 (9), 1185.
Song, K., Wang, W.Q., Yan, Y., 2019. Numerical and experimental analysis of a diffuser-augmented micro-hydro turbine. Ocean Eng. 171, 590–602.
Song, K., Yang, B., 2021. A comparative study on the hydrodynamic-energy loss characteristics between a ducted turbine and a shaftless ducted turbine. J. Mar. Sci. Eng. 9 (9), 930.
Suntivarakorn, R., Wanchat, S., Monatrakul, W., 2016. An experimental study of electricity generation using a horizontal spiral turbine. Energy Proc. 100, 532–536.
Tampier, G., Troncoso, C., Zilic, F., 2017. Numerical analysis of a diffuser-augmented hydrokinetic turbine. Ocean Eng. 145, 138–147.
Wang, X., Wang, Y., Liu, H., Xiao, Y., Jiang, L., Li, M., 2023a. A numerical investigation on energy characteristics of centrifugal pump for cavitation flow using entropy production theory. Int. J. Heat Mass Tran. 201, 123591.
Wang, X., Yan, Y., Wang, W.Q., Hu, Z.P., 2023b. Evaluating energy loss with the entropy production theory: a case study of a micro horizontal axis river ducted turbine. Energy Convers. Manag. 276, 116553.
Yang, B., Wei, K., Yang, W., Li, T., Qin, B., 2021. A feasibility study of reducing scour around monopile foundation using a tidal current turbine. Ocean Eng. 220, 108396.
Yang, F., Li, Z., Cai, Y., Jiang, D., Tang, F., Sun, S., 2022. Numerical study for flow loss characteristic of an axial-flow pump as turbine via entropy production analysis. Processes 10 (9), 1695.
Yu, Z.F., Wang, W.Q., Yan, Y., 2021. Energy loss evaluation in a Francis turbine under overall operating conditions using entropy production method. Renew. Energy 169, 982–999.
Zang, W., Zheng, Y., Zhang, Y., Lin, X., Li, Y., Fernandez-Rodriguez, E., 2022. Numerical investigation on a diffuser-augmented horizontal axis tidal stream turbine with the entropy production theory. Mathematics 11 (1), 116.
Zhang, D., Guo, P., Cheng, Y., Hu, Q., Li, J., 2023. Analysis of blockage correction methods for high-solidity hydrokinetic turbines: experimental and numerical investigations. Ocean Eng. 283, 115185.
Zhang, D., Guo, P., Qian, Y., Qiao, H., Li, J., 2024. Analysis and optimization of a deep-water in-situ power generation system based on novel ductless Archimedes screw hydrokinetic turbines. Renew. Energy 225, 120235.